Multiscale Temporal Variability of the Global Air-Sea CO 2 Flux Anomaly

Yuanyuan Gu, Gabriel Katul, Nicolas Cassar

JGR Biogeosciences

RESEARCH ARTICLE
10.1029/2022JG006934

Multiscale Temporal Variability of the Global Air-Sea CO_2 Flux Anomaly

Yuanyuan Gu[1,2], Gabriel G. Katul[3,4], and Nicolas Cassar[1,5]

[1]Division of Earth and Climate Sciences, Nicholas School of the Environment, Duke University, Durham, NC, USA, [2]College of Oceanography, Hohai University, Nanjing, China, [3]Nicholas School of the Environment, Duke University, Durham, NC, USA, [4]Department of Civil and Environmental Engineering, Duke University, Durham, NC, USA, [5]CNRS, Univ Brest, IRD, Ifremer, LEMAR, Plouzané, France

Key Points:

- Global air-sea CO_2 flux is dominated by wind effect on subseasonal time scales, on longer time scales, ΔpCO_2 effect is the main driver
- The decadal variability in global flux anomaly was almost entirely driven by ΔpCO_2 effect with highest contribution from high latitudes
- Drivers of global air-sea CO_2 flux anomaly also dominate the regional variability, particularly in the mid-high latitude oceans

Supporting Information:

Supporting Information may be found in the online version of this article.

Correspondence to:

Y. Gu,
yuanyuan.gu1@hotmail.com

Citation:

Gu, Y., Katul, G. G., & Cassar, N. (2023). Multiscale temporal variability of the global air-sea CO_2 flux anomaly. *Journal of Geophysical Research: Biogeosciences*, *128*, e2022JG006934. https://doi.org/10.1029/2022JG006934

Received 19 APR 2022
Accepted 29 MAY 2023

Abstract The global air-sea CO_2 flux (F) impacts and is impacted by a plethora of climate-related processes operating at multiple time scales. In bulk mass transfer formulations, F is driven by physico- and bio-chemical factors such as the air-sea partial pressure difference (ΔpCO_2), gas transfer velocity, sea surface temperature, and salinity–all varying at multiple time scales. To de-convolve the impact of these factors on variability in F at different time scales, time-resolved estimates of F were computed using a global data set assembled between 1988 and 2015. The F anomalies were defined as temporal deviations from the 28-year time-averaged value. Spectral analysis revealed four dominant timescales of variability in F–subseasonal, seasonal, interannual, and decadal with relative amplitude differences varying across regions. A second-order Taylor series expansion was then conducted along these four timescales to separate drivers across differing regions. The analysis showed that on subseasonal timescales, wind speed variability explains some 66% of the global F anomaly and is the dominant driver. On seasonal, interannual, and decadal timescales, the ΔpCO_2 effect controlled by the ΔpCO_2 anomaly, explained much of the F anomaly. On decadal timescales, the F anomaly was almost entirely governed by the ΔpCO_2 effect with large contributions from high latitudes. The main drivers across timescales also dominate the regional F anomaly, particularly in the mid-high latitude regions. Finally, the driver of the ΔpCO_2 effect was closely connected with the relative strength of atmospheric pCO_2 and the nonthermal component of oceanic pCO_2 anomaly associated with dissolved inorganic carbon and alkalinity.

Plain Language Summary The number of carbon dioxide (CO_2) molecules per unit surface area per unit time that enter the ocean surface from the atmosphere is quantified by the air-sea CO_2 flux (F). These CO_2 molecules impact many chemical and biological properties within the ocean. Yet, the direct controls on how many molecules can possibly be exchanged between the atmosphere and the ocean surface depend on several environmental factors such as wind speed at some reference height, the amount of CO_2 molecules in the atmosphere and in the water (or their imbalance ΔpCO_2), the wave height, and sea surface temperature. These environmental factors vary on many time scales such as daily, monthly, seasonal, annual, inter-annual, and decadal. The work demonstrates that the CO_2 gas exchange is dominated by the wind effect on subseasonal time scales, while on longer time scales, the ΔpCO_2 term, closely related to the variability of both atmospheric and oceanic CO_2, emerges as a leading driver.

1. Introduction

The global ocean currently absorbs some 25% of the annual anthropogenic CO_2 emissions and exerts a first-order control on atmospheric CO_2 and climate (Friedlingstein et al., 2020). However, significant variability as well as uncertainties in annual global net oceanic CO_2 uptake have been reported ranging from 1.19 to 2.59 Pg C yr^{-1} (Iida et al., 2021; Roobaert et al., 2018). Regionally, temperate and northern high-latitude oceans are generally associated with large net CO_2 uptake, while equatorial oceans represent major sources of CO_2 to the atmosphere (Chau et al., 2022; Takahashi et al., 2009). Temporally, variability in air-sea CO_2 fluxes (F, mol m^{-2} y^{-1}) occurs at multiple time scales ranging from fractions of seconds (where viscosity dissipates kinetic energy in eddies) to decades and centuries (climate-related processes). To average out the effects of fast processes such as turbulence and wave breaking, the CO_2 gas exchange at the air-sea interface is generally quantified by a bulk mass exchange parameterization presumed to be valid on time scales much longer than turbulence and wave breaking and is given as

Table 1
Overview of Drivers in Air-Sea CO_2 Flux F Reported in the Literature

Area	Timescale	Model/observation	Time range	Primary driver	Reference
Global	Seasonal	Model	Climatology	ΔpCO_2 driven by temperature and DIC	Lerner et al. (2021)
Arabian Sea	Seasonal	Model	Climatology	Wind speed and ΔpCO_2	De Verneil et al. (2022)
Global coastal ocean	Seasonal	Observation	1998–2015	Oceanic pCO_2 and temperature	Roobaert et al. (2019)
Arctic	Seasonal	Observation	Climatology	Temporal scale: wind speed Spatial scale: ΔpCO_2	Wrobel (2017)
South western Atlantic	Seasonal	Model	Climatology	Oceanic pCO_2 driven by temperature and DIC	Arruda et al. (2015)
Global	Seasonal, interannual	Observation	1998–2011	Oceanic pCO_2	Landschützer et al. (2014)
Global	Interannual	Model	1979–2004	Oceanic pCO_2 driven by DIC	Doney et al. (2009)
Southern Ocean	Interannual	Model	1958–2004	Oceanic pCO_2 driven by DIC	Lovenduski et al. (2007)
Equatorial Pacific	Interannual	Model	1979–1997	Oceanic pCO_2 driven by DIC	Le Quéré et al. (2000)
Global	Decadal	Observation	1982–2011	Subtropical: CO_2 solubility driven by temperature; high-latitude: DIC and ALK	Landschützer et al. (2016)
North Atlantic	Interannual to multidecadal	Model	1950–2099	Interannual and shorter timescale: ΔpCO_2 and k; pentadal to multidecadal: ΔpCO_2	Couldrey et al. (2016)
Global	Trend	Model	1990–2009	Temperature; atmospheric pCO_2	Sitch et al. (2015)

$$F = k \times K_0 \times \Delta pCO_2 = k \times K_0 \times (pCO_{2o} - pCO_{2a}), \quad (1)$$

where a positive (negative) F represents out- (in-) gassing of CO_2. The K_0 is the solubility of CO_2 (mol L^{-1} atm^{-1}) and varies with sea surface temperature (SST) and salinity (Weiss, 1974), k is the gas transfer velocity (cm h^{-1}) and encodes all the complexity of the air-water mass exchange process due to turbulence and wave breaking related processes, and ΔpCO_2 (µatm) is the difference in partial pressures of CO_2 between the ocean (pCO_{2o}) and the atmosphere (pCO_{2a}). The k term is regulated by turbulence intensity near the air-sea interface arising from wind stresses and buoyancy effects among other factors (Jähne et al., 1985; Komori et al., 1993; Sarmiento & Gruber, 2006). For simplicity, climate models typically parameterize k as a function of readily accessible parameters, the common one being the mean wind speed at 10 m above the water surface (McGillis et al., 2004; Nightingale et al., 2000; Prytherch et al., 2010; Wanninkhof, 1992, 2014). Other processes such as waves, breaking waves, bubbles, and sea spray can also mediate the magnitude of k and their effects have been accommodated to some extent in other wind-wave parameterizations of k (Brumer et al., 2017a; Brumeret al., 2017b; Deike & Melville, 2018; Goddijn-Murphy et al., 2011; Staniec et al., 2021; Zhao & Toba, 2001).

Prior work on the processes driving variability in F has been restricted to regional scales or limited by specific timescales. Moreover, owing to the relatively sparse observations of pCO_2 in time and space, prior studies generally relied on global or regional model simulations to assess the modes of variability in F and the processes that control them. A complete review of all the relevant literature goes beyond the scope of a single study, but a few studies are summarized in Table 1. Typically, both model- and observation-based studies underscore that the seasonal cycles of F in regional oceans (e.g., low latitude oceans in both hemispheres, high-latitude North Pacific, Atlantic Ocean, Southern Ocean, and Indian Ocean) are primarily driven by oceanic pCO_2 associated with temperature and dissolved inorganic carbon (DIC) under the impact of biogeochemical and physical processes or factors such as photosynthesis, temperature, and upper water mixing (Landschützer et al., 2014, 2018; Lerner et al., 2021; Long et al., 2013; Takahashi et al., 1997, 2002). On interannual timescales, both ΔpCO_2 and k are needed to explain the variability in F (Couldrey et al., 2016). The variability of the oceanic physical environment (e.g., SST, wind stress, ocean circulation, and water column mixing) at this timescale has a significant impact on the ΔpCO_2 and k. For example, the oceanic pCO_2, a main driver of ΔpCO_2 (Takahashi et al., 2002), has been shown to be primarily affected by DIC concentration associated with ocean circulation (Doney et al., 2009; Long et al., 2013; Lovenduski et al., 2007). For variations on longer timescales, F is mainly controlled by ΔpCO_2 with k contributing modestly (e.g., 25% in the North Atlantic; Landschützer et al., 2016; Couldrey et al., 2016; Mckinley et al., 2011).

The objective here is to identify the mechanisms driving the global air-sea CO_2 flux variability at multiple timescales (i.e., subseasonal, seasonal, interannual, and decadal timescales) derived from a recent global data product that allows the estimation of F. The work builds on the studies presented in Table 1 using new observation-based products with the goal to discern to what extent understudied processes or factors such as wave breaking, SST, wind speed, and pCO_2 individually and jointly (i.e., act in coordination with other processes) shape F anomalies at multiple scales over time. To this end, recently compiled temporally resolved global data sets from 1988 through 2015 assembled on

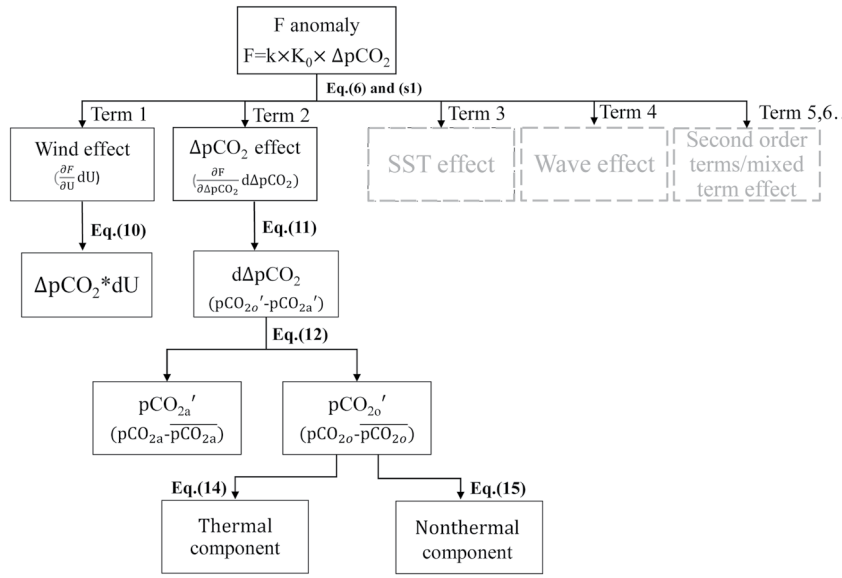

Figure 1. Schematic diagram illustrating the physical mechanisms, procedures, and associated equations to be considered in quantifying the variability in F. The SST effect, wave effect, and higher order terms are shown in gray because of their minor contributions to the F anomaly (Figure S1 in Supporting Information S1). The diagram is further described in the following sections.

a spatial resolution of 0.5° × 0.5° are used. These data sets enable the computation of F at multiple time scales (monthly to decadal) using models for *k* forced by different mechanisms. At first-order, variability in F at different time scales and regions must reflect the strength and variability of its dominant drivers. Addressing this question opens up new perspectives about global climate model evaluation, guiding efforts to undertake field campaigns and long-term monitoring initiatives, and perhaps offering a new categorization of regional oceans in terms of their controls on F variability at differing time scales. The manuscript is organized as follows: the data sources and methods are introduced in Section 2. In Section 3, a second order Taylor series expansion is applied to separate the drivers (effect of wind speed, ΔpCO_2, SST, and wave height) of CO_2 flux variability on four spectrally energetic timescales while including all the joint effects of the drivers. The main procedures and related equations are schematically illustrated in Figure 1. Limitations and conclusions are presented in Sections 4 and 5, respectively.

2. Data and Method

2.1. Data Product and Processing Method

Wind speed (U), SST, significant wave height (H_s), sea surface salinity, and ΔpCO_2 data are applied to estimate the CO_2 flux and evaluate the drivers of its variability over a period from 1988 to 2015. All data products are linearly interpolated onto a spatial resolution of 0.5° × 0.5°.

To reduce the uncertainty sourced from wind product when using the wind-dependent parameterization from Wanninkhof (2014), monthly 0.25° × 0.25° Cross-Calibrated Multi-Platform (CCMP) V2.0 wind speed data at 10-m height (Atlas et al., 2011; Hoffman et al., 2013) are obtained from Remote Sensing System. The monthly SST and H_s data at a resolution of 0.5° × 0.5° are obtained from the European Centre for Medium-Range Weather Forecasts (ECMWF) fifth generation ERA5 reanalysis products (Hersbach et al., 2018), a globally complete and consistent data set combining model data with observations across the world. The empty values of H_s in polar regions (mainly in ice-covered regions) are set to zero. The monthly ΔpCO_2, atmospheric pCO_2 and oceanic pCO_2 data at a resolution of 1° × 1° are from SOM-FFN (Self-Organizing Map-Feed-Forward Network) products, and the oceanic pCO_2 data set is developed using a neural-network method (Landschützer et al., 2016, 2017). This product is based on observational oceanic pCO_2 from the Surface Ocean Carbon Atlas (SOCAT) version 2 database (Bakker et al., 2014). However, the spatial-temporal smoothing in the SOM-FFN pCO_2 product filters out high-frequency variability in some regions, potentially leading to an underestimation of subseasonal timescales.

For this reason, all the analyses here have been repeated using an ensemble pCO_2 product-SeaFlux data set (Gregor & Fay, 2021). It was found that the main results are unaltered (as shown in Supporting Information S1). The monthly climatological sea surface salinity data at 1° × 1° resolution is from the World Ocean Atlas 2009 (WOA09) described elsewhere (Antonov et al., 2010).

2.2. Calculation of the Gas Transfer Velocity (k)

To assess the robustness of the results, two different parameterizations are used to estimate k. The widely used wind-only relation (labeled as k_{W14}) is from Wanninkhof (2014) and is expressed as

$$k_{W14} = aU^2(\mathrm{Sc}/660)^{-1/2}, \tag{2}$$

where $a = 0.251$ in unit of (cm hr^{-1}) (m s^{-1})$^{-2}$, and Sc is the molecular Schmidt number for CO_2 assumed to be a function of SST only (Wanninkhof, 2014).

The second expression depends on both wind and wave conditions (Deike & Melville, 2018). This parameterization (labeled as k_{D18}) explicitly considers the bubble effect and is given as

$$k_{D18} = u_*\left[A_{NB}\left(\frac{\mathrm{Sc}}{660}\right)^{-1/2} + \frac{A_B}{W_0}\left(\left(u_* {c_{wh}}^2\right)^{2/3}\right)\right]. \tag{3}$$

In this equation, u_* is the air-side friction velocity, which is estimated from a quadratic drag force relation $u_* = U {C_D}^{1/2}$, where U (m s^{-1}) is the near-neutral mean wind speed at 10 m and C_D is a drag coefficient defined at 10 m height above the water surface, which can be estimated from $C_D = (2.7U^{-1} + 0.142 + 0.076U) \times 10^{-3}$ (Large, 2006). The A_{NB} is a dimensionless constant given as 1.55×10^{-4}, $A_B = 1 \pm 0.2 \times 10^{-5}$ m^{-2} s^2, W_0 is the dimensionless Ostwald solubility coefficient, expressed as $W_0 = K_0RT$, R is the ideal gas constant (Keeling, 1993), $c_{wh} = \sqrt{gH_s}$ is the ballistic speed, g is the gravitational acceleration ($g = 9.8$ m s^{-2}), and H_s is the significant wave height that must be externally supplied here. Ice-covered and coastal oceans within 1° of the coastline were not included in the calculations because the spatial coverage of the SOM-FFN pCO_2 product is coarse in these regions. The global averaged CO_2 flux is computed to be around −1.39 Pg C yr^{-1} from K_{W14} and −1.58 Pg C yr^{-1} from K_{D18}, and both estimates are within the range reported in the literature (Iida et al., 2021; Roobaert et al., 2018).

2.3. Fourier Spectral Analysis of the Air-Sea CO_2 Flux (F)

Variability in F at multiple time scales is analyzed using Fourier spectral analysis. Both power spectrum $E(f)$ and energy spectrum $f\,E(f)$ as a function of frequency f are presented. The power spectrum satisfies the normalizing property $\int_0^\infty E(f)df = {\sigma_F}^2$, where σ_F is the temporal standard deviation of F. Because $E(f)$ measures the variability per unit frequency, $f\,E(f)$ measures variability (or activity) adjusted by frequency or inverse time scale at f. In typical time-series where high frequency contains small $E(f)$ and low frequency contains high $E(f)$, the product $f\,E(f)$ is intended to measure variability or activity adjusted by size or inverse time scale. This so-called "pre-multiplied" spectrum $f\,E(f)$ is routinely used in geophysical flows (e.g., Stull, 1988) to discern transitions between white-noise (i.e., $E(f) \sim f^0$) and power-laws ($E(f) \sim f^{-\alpha}$, $\alpha > 1$) as this transition frequency corresponds to the peak (or maximum) in the product $f\,E(f)$. Moreover, under certain conditions (e.g., a Lorentzian spectrum), this peak is connected to the "memory" (or integral time scale) in the series. The spectral analysis here is conducted in two ways. The first approach, which we call "mass-preserving" approach, computes a global monthly F by averaging across all 0.5° × 0.5° grid cells thereby resulting in a single monthly globally averaged F time-series over the entire 28-year record. Spectral analysis can then be conducted on this spatially averaged F record so as to identify dominant energetic time scales in such a spatially averaged F time-series. This approach preserves the overall computed global CO_2 mass flux between the ocean and the atmosphere. A drawback of this approach is that spatial averaging across grid cells dampens F temporal variability originating from space that may have some memory effects (or legacy) at later times. For this reason, a second approach is introduced and is labeled as "variance-preserving." In this second approach, spectral analysis on the time-series of F for each 0.5° × 0.5° grid cell is first conducted. At each frequency, the squared Fourier amplitudes are computed for each grid cell and their mean across space for each f is tracked. Because variances are additive, this approach preserves the spatial variability at each frequency and when integrated across frequencies, preserves the overall (space-time) variance in F. A drawback of this approach is that the local spectra at each 0.5° × 0.5° grid cell are

computed after removal of local means in time. As such, information about the overall global F sinks or sources is partially lost. For this reason, both approaches are used and compared to assess whether the dominant time scales are robust to the spectral method of analysis.

Once these dominant time scales are identified, the variability in F and driving factors are analyzed at those individual time scales. To extract specific timescales of these time-series, the original monthly F and the associated driving factor time-series in each $0.5° \times 0.5°$ grid was first transformed into the frequency domain using Fast Fourier Transforms. Squared Fourier amplitudes not associated with the target frequency (or range of frequencies) to be studied are set to zero. However, all phase angles derived from the Fourier transform are unaltered. An inverse Fourier transform is then applied to reconstruct the real part of the time-series at this target time scale. The relations between F and its drivers constructed at this target time scale are then studied. It should be noted that Fourier decomposition method may induce some biases at the edges (beginning and end) of the time-series as is the case for the reconstruction of any finite series. Fourier analysis assumes periodic boundary conditions, which can be problematic when the original time-series shows some long-term trends (e.g., atmospheric pCO_2). Other methodological approaches such as wavelets and empirical mode decomposition (EMD) can also be used to extract the temporal signal of CO_2 flux and assess modes of variability (Landschützer et al., 2016; Zhang et al., 2022). Understandably, each method does have its strengths and limitations. For example, the selection of a wavelet basis function also incurs uncertainty at edges depending on the assumptions used in the wavelet transform (periodic boundaries, mirror-image, etc.). Depending on the time-frequency localization of the analyzing wavelet, energy leakages across scales are unavoidable when precise frequencies are also sought. The EMD is also sensitive to both—the record length and edge effects. Because EMD is utilized entirely in the time domain, multiple periodicities that are adjacent to each other in the frequency domain lead to "mode-mixing," which can be problematic for the application here. Differences among these methods are certainly a topic that warrants inquiry and is better kept for the future.

2.4. Drivers of Air-Sea CO_2 Flux (F): A Taylor Series Expansion Analysis

To evaluate the contribution of each driver to the interannual variability of F and accommodate any interactions among them across scales, a second order Taylor series expansion is applied to the annual averaged Fourier reconstructed time-series in each grid at four target time scales. Annual average salinity in each grid was applied due to its comparatively small effects on F (Lovenduski et al., 2007; Sarmiento & Gruber, 2006). The F estimated using the k_{W14} expression (F_{W14}) is a function of three variables: wind speed, ΔpCO_2 and SST, so that

$$F_{W14} = f\,(U, \Delta pCO_2, SST). \tag{4}$$

Changes in F_{W14} ($=dF_{W14}$) are the annual averaged F_{W14} anomaly estimated by subtracting long-term average F_{W14} (indicated by overline) from the annual averaged F_{W14} for each grid and is given as

$$dF_{W14} = F_{W14} - \overline{F_{W14}}. \tag{5}$$

Using a second order Taylor series expansion, it is related to its drivers via

$$\begin{aligned} dF_{W14} = &\Bigg[\underbrace{\frac{\partial F_{W14}}{\partial U}dU}_{\text{Term1}} + \underbrace{\frac{\partial F_{W14}}{\partial \Delta pCO_2}d\Delta pCO_2}_{\text{Term2}} + \underbrace{\frac{\partial F_{W14}}{\partial SST}dSST}_{\text{Term3}}\Bigg] + \Bigg[\underbrace{\frac{1}{2!}\frac{\partial^2 F_{W14}}{\partial U^2}dU^2}_{\text{Term4}} + \underbrace{\frac{1}{2!}\frac{\partial^2 F_{W14}}{\partial \Delta pCO_2{}^2}d\Delta pCO_2{}^2}_{\text{Term5}} \\ &+ \underbrace{\frac{1}{2!}\frac{\partial^2 F_{W14}}{\partial SST^2}dSST^2}_{\text{Term6}} + \underbrace{\frac{\partial^2 F_{W14}}{\partial U \partial \Delta pCO_2}dU\,d\Delta pCO_2}_{\text{Term7}} + \underbrace{\frac{\partial^2 F_{W14}}{\partial U \partial SST}dU\,dSST}_{\text{Term8}} + \underbrace{\frac{\partial^2 F_{W14}}{\partial \Delta pCO_2 \partial SST}d\Delta pCO_2 dSST}_{\text{Term9}}]. \end{aligned} \tag{6}$$

Here, Term1 + Term4, Term2 + Term5, and Term3 + Term6 represent the effects of wind speed, ΔpCO_2, and SST, respectively. The sum of mixed terms Term7 + Term8 + Term9 signifies "joint effects," measuring the nonlinear (i.e., quadratic) contribution impacting dF_{W14} (Igarashi et al., 2015). Similarly, for F estimated using k_{D18} expression (F_{D18}), the additional contribution of H_s must be considered, so that

$$F_{D18} = f(U, \Delta pCO_2, SST, H_s), \tag{7}$$

and

$$dF_{D18} = F_{D18} - \overline{F_{D18}}. \quad (8)$$

The resulting second order Taylor series expansion is also given (Text S1 in Supporting Information S1).

We focus our analyses on k_{W14} because of the similarity in the results when using k_{D18} (see Supporting Information S1).

3. Results and Discussion

The spectra of the computed monthly F are analyzed to assess the dominant modes of variability in two ways (mass vs. variance averaging). Once these key energetic modes or frequencies are identified, time-series of F and its drivers are then reconstructed at those particular time scales. The second order Taylor series expansion is then applied to analyze the contribution of each driver to F anomaly and its associated variability at those energetic time scales. The processes leading to the variability of the identified drivers on different time scales are further analyzed.

3.1. Multiscale Variability of Air-Sea CO_2 Flux

For simplicity, we refer to $E(f)$ as the power spectrum (i.e., units of variance per unit frequency) and its pre-multiplied form $f\,E(f)$ as the energy spectrum (units of variance). The power (averaged energy) and energy spectra produced by the "mass-preserving" approach are generated from spatially averaging CO_2 fluxes and their associated driving variables across all grid cells (Figures 2a and 2b). The spectra are compared against the "variance-preserving" approach that generates the spectra of F and driving variables for each grid cell and then spatially averages all spectra for each frequency (Figures 2c and 2d). For the "variance-preserving" approach, the spatial coefficient of variation ($=\sigma/\mu$, where σ is standard deviation of the spatial energy, μ is the spatially averaged energy) at each frequency can be determined (Figures 2e and 2f). In all spectral calculations, the F_{W14} and F_{D18} results are further compared.

The spectra for F_{W14} and F_{D18} are almost indistinguishable at all time scales (Figure 2). The power spectra for all variables from the mass- and variance-preserving approaches are similar though the contained power per frequency is different (Figures 2a and 2c). In contrast, energy spectra from the two approaches differ in distribution and magnitude (Figures 2b and 2d). However, similar multiscale variability among the two approaches is evident for F and the driving factors (wind speed, ΔpCO_2, SST, and H_s). Both mass- and variance-preserving approaches agree that two peaks on timescales of annual (~12 months) and semiannual (~6 months) are the dominant modes of variability in the F spectra, which is consistent with prior studies (e.g., Wanninkhof et al., 2013).

The power is lowest in subseasonal timescales (<3 months) and highest in decadal (>10 years) or seasonal (6–12 months) timescales depending on averaging approaches. In contrast, the total energy retained in seasonal timescales is 12 times higher than that in decadal and subseasonal timescales, and in interannual timescales (2–7 years) the retained energy is the lowest for the "mass-preserving" approach. For the "variance-preserving" approach, though the highest total energy is also observed in seasonal timescales, the subseasonal timescales contain the second highest energy, which are much larger than the energy in decadal timescales. Therefore, though the most energetic mode is seasonal variability, the second most energetic mode is decadal or subseasonal variability depending on the averaging approaches. Because variances from the "variance-preserving" approach are additive, the integrated energy and power are larger than those from the "mass-preserving" approach. Energy in "mass-preserving" approach decreases more in the high frequencies than "variance-preserving" approach due in large part to the regionally generated spatial variability at high frequencies (Fredriksen & Rypdal, 2016), particularly in the subseasonal timescales. This finding also indicates that aliasing effect has much weaker signature on the variance-preserving approach when all the spectra are averaged out because aliasing cannot act identically on each grid cell given the dissimilarity in the finer-scale processes. Interestingly, the coefficient of variation suggests highest spatial variability occurs on the 6-month time scale (Figures 2e and 2f). In all cases, the spatial variability exceeds the mean energy content at every frequency analyzed—though the coefficient of variation is surprisingly bounded within a narrow range (1.2–2.2 for power spectra and 2–3.2 for energy spectra). Overall, while the mass-preserving and variance-preserving approaches differ in some ways, they both highlight

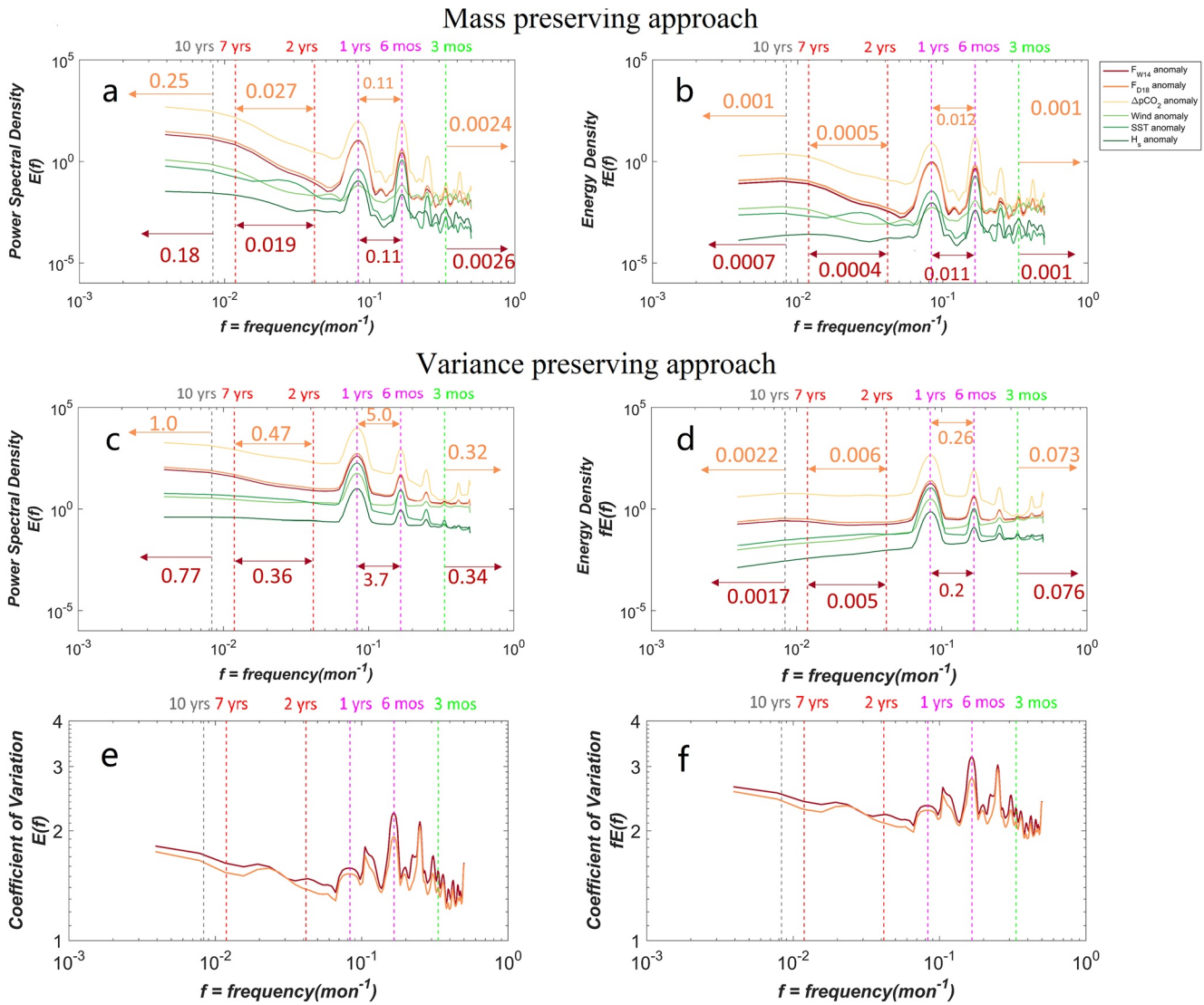

Figure 2. Global averaged (a) power spectral density $E(f)$ and (b) energy spectra f $E(f)$ for CO_2 flux anomaly from both expressions (F_{W14} and F_{D18}) and relevant variables (anomalies in ΔpCO_2, wind speed, sea surface temperature (SST) and significant wave height (H_s)) (from mass preserving approach). (c) Spatially averaged power spectral density and (d) energy spectra for F_{W14} and F_{D18} anomalies and relevant factors at each grid (from variance preserving approach). Coefficient of variation of the spatial variability in (e) power spectra $E(f)$ and (f) energy spectra f $E(f)$ of F_{W14} and F_{D18} as a function of frequency. For (b) and (d), energy on the y-axis is estimated by multiplying the power spectral density with the frequency (i.e., pre-multiplied representation). The dashed vertical lines represent the timescales as labeled and the values are the energy contained (also the variance) in the corresponding timescales. From right to left, the lines represent subseasonal (<3 months), seasonal (6 months–1 year), interannual (2–7 years) and decadal timescales (>10 years).

dominant energy at subseasonal, seasonal, interannual, and decadal timescales. We therefore interrogate these specific timescales using the Taylor series expansions. These selected "target" scales also span all the time scales considered or deemed as significant in Table 1.

The energy or activity on interannual timescales may be associated with the El Niño–Southern Oscillation (ENSO), with correlation coefficients (R) between the Niño 3.4 index and average CO_2 fluxes over the global ocean and within tropical region being around −0.6 and −0.8, respectively (Figure S2a in Supporting Information S1). ENSO, which generally occurs every 2–7 years, governs the interannual variability of CO_2 flux over the global ocean though it occurs within the tropical Pacific (Feely et al., 1999; Ishii et al., 2014; McKinley et al., 2004). During the warm phase of ENSO, trade wind speed reduces, and upwelled DIC decreases due to the weakened upwelling and deepened thermocline in the eastern Pacific, leading to less CO_2 outgassing. In contrast, stronger winds and more DIC transported to the ocean surface drive more CO_2 outgassing of the ocean.

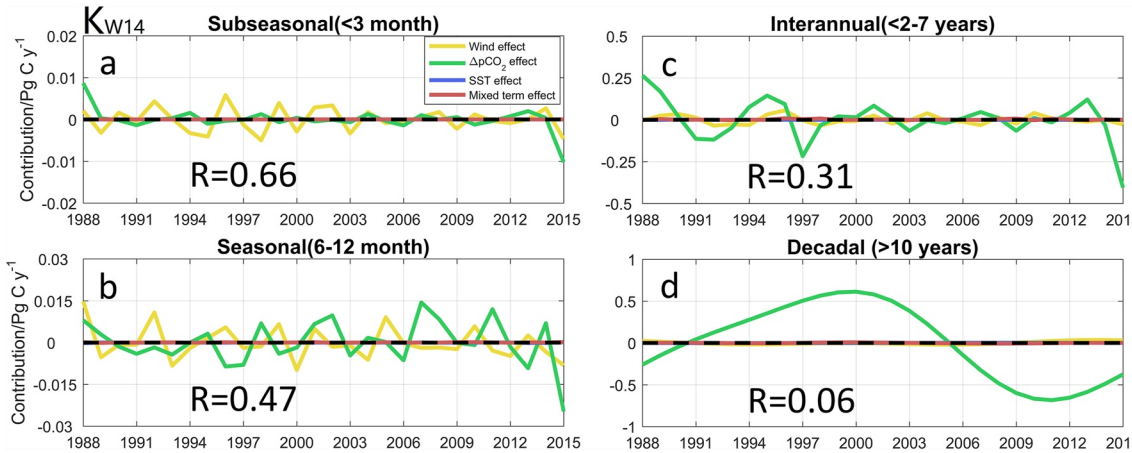

Figure 3. Time-series of each terms' contribution (wind, ΔpCO_2, SST and the sum of the mixed terms) to the CO_2 flux anomaly based on k_{W14} from 1988 to 2015. (a)–(d) show subseasonal, seasonal, interannual, and decadal timescales, respectively. The R terms are calculated using Equation 9. Contributions of SST and the summed mixed terms are small and indistinguishable from the x-axis.

The Pacific Decadal Oscillation (PDO) is a major driver of decadal variability of physical and biological activity in the Pacific Ocean. It can modulate regional and even global CO_2 flux by impacting oceanic pCO_2 (Feely et al., 2006; Takahashi et al., 2003). This connection is supported by the correlation coefficients between the PDO index and global F ($R = 0.7$) and average F in mid-high latitude regions ($R > 0.8$) (Figure S2b in Supporting Information S1). Some energy on scales shorter than 3 months might be linked to the Maddan-Julian Oscillation (MJO), though correlation between global F and MJO index is low (not shown). The MJO, which reflects large-scale coupling between tropical deep convection and atmospheric circulation, has a large impact on tropical wind speeds (Madden & Julian, 1971). An explicit connection between the MJO and global CO_2 flux is understudied compared to PDO and ENSO but the spectra from the variance-preserving approach highlight variability on subseasonal timescales. Therefore, the subseasonal timescales are included in this analysis. Though other climate modes (e.g., Atlantic Multidecadal Oscillation, Southern Annular Mode or North Atlantic Oscillation) do not show a clear relation to the global CO_2 flux, their influences on the variability of regional CO_2 flux are verified by both models and observations (Landschützer et al., 2015; McKinley et al., 2017).

3.2. Mechanisms Explaining the CO_2 Flux Anomaly Across Scales

Wind and ΔpCO_2 effects are two major drivers of the variability in the F anomaly. Contributions of SST, H_s and the nonlinear mixed terms appear to be small and are neglected for all four timescales at global spatial scales (Figure 3; Figure S3 in Supporting Information S1). The negligible contribution of SST and H_s might be attributable to the small effect of these two terms on F compared with wind speed and ΔpCO_2 (Figure S4a in Supporting Information S1). Though both Sc and CO_2 solubility vary with SST, the counteracting response of F to $(Sc/660)^{-0.5}$ and solubility dampens the response of F to SST variations (Figure S4b in Supporting Information S1). While the direct effect of SST on F is small, its indirect impact on F through oceanic pCO_2 is large at regional scales (Lerner et al., 2021; Roobaert et al., 2019). The annual variability of wind speed and ΔpCO_2 effects are consistent for both expressions, though their magnitudes differ by negligible amounts. A dimensionless ratio is now introduced to evaluate the relative importance of wind speed and ΔpCO_2 effects on F variability for each of the four timescales. The ratio is labeled as R and is given by

$$R = \frac{|\text{wind effect}|}{|\Delta pCO_2 \text{ effect}| + |\text{wind effect}|}, \tag{9}$$

where |.| represents the absolute value of each term. For example, the $R = 0.5$ represents an equal wind and ΔpCO_2 effect, while the closer the ratio is to 0, the more influence the ΔpCO_2 effect has, and the closer the ratio is to 1, the more influence the wind effect has. The quantification of the wind effect on F based on Equation 6 is expressed as

$$\frac{\partial F_{W14}}{\partial U} dU + \frac{1}{2!} \frac{\partial^2 F_{W14}}{\partial U^2} dU^2 = 0.502 a U (\Delta pCO_2)(Sc/660)^{-1/2} dU + 0.251 (\Delta pCO_2)\, dU^2 \tag{10}$$

Table 2
Regional Variations in the Factor (Wind vs. pCO_2) That Predominantly Controls Air-Sea CO_2 Flux (F_{W14}) Variability at Four Timescales

Zones	Time scales			
	Subseasonal	Seasonal	Interannual	Decadal
Tropical (15°S–15°N)	$\text{Wind}\vert_{R=0.81}$	$\text{Wind}\vert_{R=0.57}$	$\Delta pCO_2\vert_{R=0.28}$	$\text{Wind}\vert_{R=0.61}$
Northern temperate (15°N–45°N)	$\text{Wind}\vert_{R=0.68}$	$\Delta pCO_2\vert_{R=0.48}$	$\Delta pCO_2\vert_{R=0.41}$	$\Delta pCO_2\vert_{R=0.24}$
Arctic (45°N–75°N)	$\text{Wind}\vert_{R=0.75}$	$\text{Wind}\vert_{R=0.53}$	$\Delta pCO_2\vert_{R=0.41}$	$\Delta pCO_2\vert_{R=0.05}$
Southern temperate (15°S–45°S)	$\text{Wind}\vert_{R=0.68}$	$\text{Wind}\vert_{R=0.51}$	$\Delta pCO_2\vert_{R=0.41}$	$\Delta pCO_2\vert_{R=0.2}$
Southern Ocean (45°S–75°S)	$\Delta pCO_2\vert_{R=0.37}$	$\Delta pCO_2\vert_{R=0.37}$	$\Delta pCO_2\vert_{R=0.21}$	$\Delta pCO_2\vert_{R=0.03}$
Global oceans	$\text{Wind}\vert_{R=0.66}$	$\Delta pCO_2\vert_{R=0.47}$	$\Delta pCO_2\vert_{R=0.31}$	$\Delta pCO_2\vert_{R=0.06}$

Note. The ratio R from Equation 9 for each region is presented.

and the ΔpCO_2 effect in Equation 6 is expressed as

$$\frac{\partial F_{W14}}{\partial \Delta pCO_2} d\Delta pCO_2 + \frac{1}{2!}\frac{\partial^2 F_{W14}}{\partial \Delta pCO_2{}^2} d\Delta pCO_2{}^2 = 0.251 a U^2 (Sc/660)^{-1/2} d\Delta pCO_2. \quad (11)$$

The averaged R marginally differ with different k parameterizations for each time scale. Calculations based on k_{D18} predict relatively higher ΔpCO_2 effect and lower wind effect (Figure S3 in Supporting Information S1). From subseasonal to decadal time scales, ΔpCO_2 effect plays an increasingly important role in determining F variability, and conversely the variability in the contribution of wind effect decreases when compared with ΔpCO_2 effect. The wind effect is stronger than ΔpCO_2 effect only on subseasonal time scales. Neglecting the contributions from other factors, the contribution from wind at subseasonal time scales is about twice as large as the ΔpCO_2 effect, with the wind effect accounting for approximately 66% of CO_2 flux variability, and the ΔpCO_2 effect contributing the remaining 34%. On seasonal timescales, contributions from wind are slightly smaller than ΔpCO_2 effect ($R = 0.47$ for k_{W14}; $R = 0.39$ for k_{D18}). In contrast, the variability of CO_2 flux is dominated by the ΔpCO_2 effect on interannual timescales ($R \approx 0.3$) and is almost entirely driven by ΔpCO_2 effect on decadal timescales ($R \approx 0.05$).

Considering the possible counteracting regional effects of each factor on global averaged CO_2 flux anomaly, Hovmöller diagrams of these drivers on four timescales throughout the study period are now presented (Figure 4; Figure S5 in Supporting Information S1). The zonal distributions of each factor's effect based on the two k expressions show small differences over years (excluding the contribution of H_s). Across the global ocean, wind and ΔpCO_2 effects play a major role in controlling the global variability of CO_2 flux and the effects of SST and H_s are negligible. Regionally, the magnitude of wind and ΔpCO_2 effects vary with latitude across scales. The dominant drivers of variability in regional F_{W14} across scales are summarized (Table 2). To some extent, the main drivers on global scales also dominate the regional variability in CO_2 flux anomaly. In tropical regions (15°S–15°N), wind effect is the main driver of F variability across scales except at interannual scales. In southern temperate (15°S–45°S) and Arctic (45°N–75°N) regions, the wind effect dominates the F variability on subseasonal and seasonal timescales and ΔpCO_2 effect is the main driver on interannual and decadal timescales. In northern temperate oceans (15°N–45°N), the ΔpCO_2 effect is the primary driver across scales except at subseasonal timescales, while in the Southern Oceans (45°S–75°S), F variability is predominantly controlled by the ΔpCO_2 effect. On seasonal to decadal timescales, the Southern Ocean is unique and often the main driver of the global patterns observed in F anomaly. Conversely, on subseasonal timescales, the dominant role of the wind effect on variability in global F results from regions other than the Southern Ocean, with the largest contribution coming from the tropical regions (81%). We also note that on decadal time scales, the ΔpCO_2 effect, and the resulting F anomalies at high latitudes (south of 45°S or north of 45°N) experience a dramatic increase from 1988 to 2000, followed by a reduction to negative after 2005 (Figure 4, bottom).

The results here show some similarities with recent model- and observation-based studies (Table 1). The ocean general circulation model runs by Couldrey et al. (2016) show that the CO_2 flux variability in the North Atlantic Ocean is predominantly produced by the effect of ΔpCO_2 rather than gas transfer velocity on pentadal to mutidecadal timescales. Landschützer et al. (2015) also emphasized the dominant role of ΔpCO_2 in the decadal variability

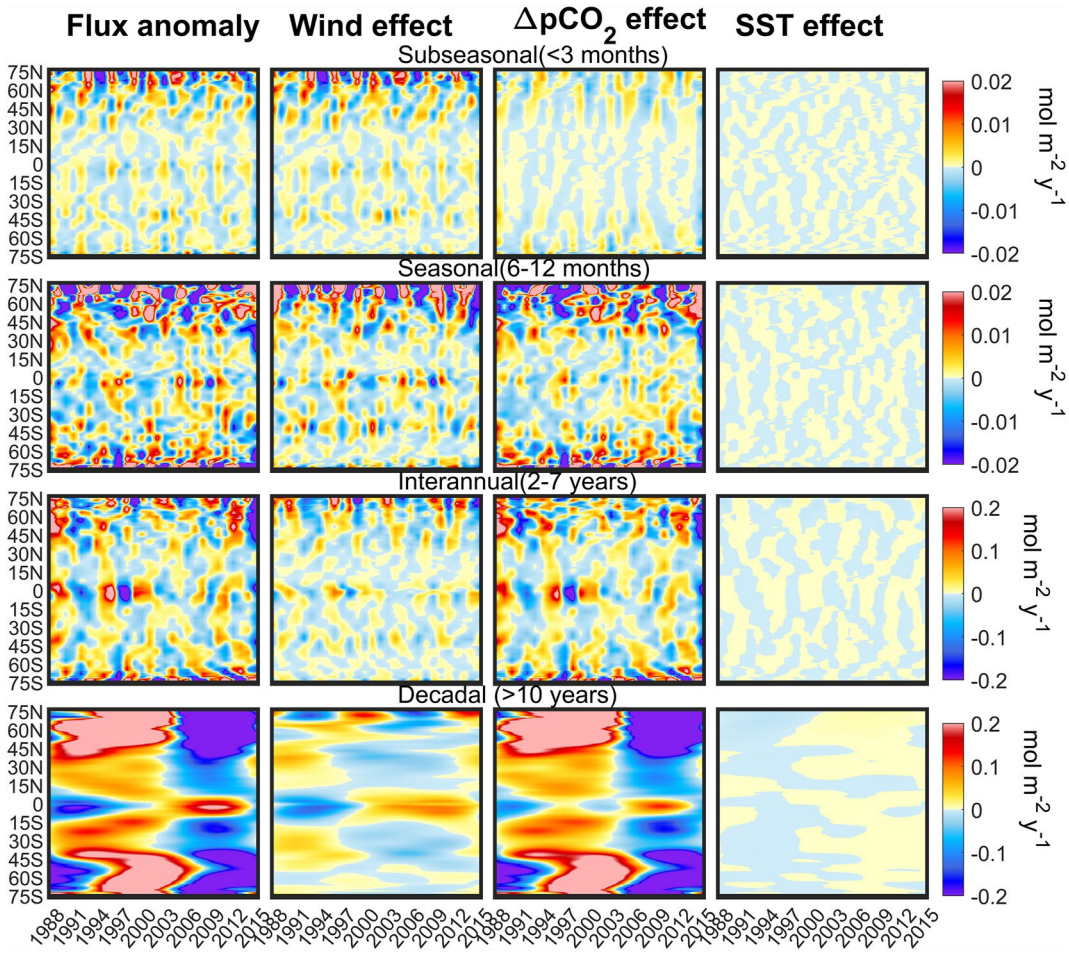

Figure 4. Hovmöller diagrams of the distribution of each term's contribution to the CO_2 flux anomaly from 1988 to 2015 at various timescales for k_{W14} (from top to bottom, subseasonal, seasonal, interannual, and decadal timescales). (First column) flux anomaly; (second column) wind speed effect; (third column) ΔpCO_2 effect; (fourth column) SST effect.

of CO_2 flux in Southern Ocean. These findings are supported by the global analysis here. The seasonal variability in Arctic air-sea CO_2 flux dominated by wind speed is in line with the observations from Wrobel (2017). Regional variations in the relative contribution of wind and ΔpCO_2 to the seasonality of F was also revealed by the modeling study of Lerner et al. (2021). On longer timescales, the dominant role of ΔpCO_2 in determining the interannual and decadal variability in global air-sea CO_2 flux has been reported based on modeling (Doney et al., 2009) and observational (Landschützer et al., 2016) studies. The observation-based work here corroborates these earlier results, comprehensively expanding from subseasonal to decadal timescales for the study of air-sea CO_2 flux and its drivers at the global and regional scales.

In addition to evaluating these drivers of the air-sea CO_2 flux variability, it is also necessary to investigate the main causes for the wind and ΔpCO_2 effect. Intuitively, based on Equation 10 and in light of the negligible effect of the second order term (Figures S1 and S6 in Supporting Information S1), the wind effect on F is determined by the states of the long-term average U, SST, ΔpCO_2, and dU (where dU is the difference between the annual average U and long-term average U). The terms U and Sc are positive and only change the magnitude of the wind effect. Therefore, whether the wind effect induces a positive or a negative anomaly in the CO_2 flux is controlled by the anomaly product $\Delta pCO_2 * dU$ (a form of coordination between the wind anomaly and the concentration gradient with the atmosphere i.e., implied when these drivers are either in phase or out of phase). As expected, the latitude-time distributions of $\Delta pCO_2 * dU$ (Figure 5, left) over time are in good agreement with the wind effect (Figure 4, middle left).

Clearly, based on Equation 11 the magnitude of ΔpCO_2 effect is determined by the long-term average U, SST, and the term $d\Delta pCO_2$. The $d\Delta pCO_2$ is estimated by subtracting the long-term average ΔpCO_2 from the annual

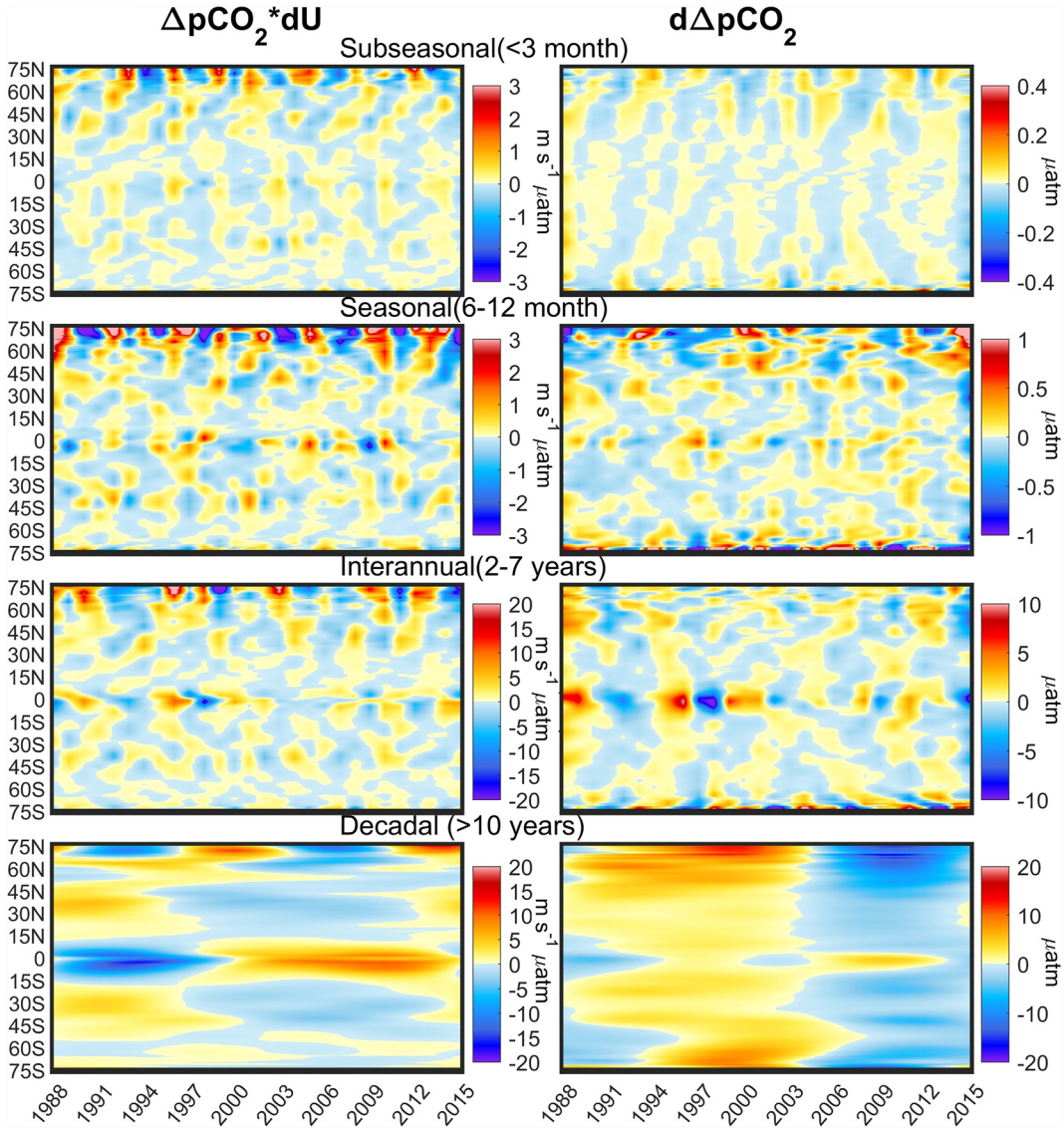

Figure 5. Hovmöller diagrams of the distribution of the term ΔpCO_2 multiplied by wind anomaly (ΔpCO_2 * dU, left) and $d\Delta pCO_2$ (right) from 1988 to 2015 at various timescales (from top to bottom, subseasonal, seasonal, interannual, and decadal timescales).

average ΔpCO_2 (i.e., $\Delta pCO_2 - \overline{\Delta pCO_2}$). Because of the positive value of U^2 and Sc, the variability of zonal distribution ΔpCO_2 effect (Figure 4, middle right) over time is governed by $d\Delta pCO_2$ (Figure 5, right). Similarly, latitude-time distributions of wind and ΔpCO_2 effects based on k_{D18} are also dominated by the variation in ΔpCO_2 * dU and $d\Delta pCO_2$, respectively (Figure S5 in Supporting Information S1; Figure 5).

3.3. Drivers of $d\Delta pCO_2$ Across Scales

As shown in the analyses above, the $d\Delta pCO_2$ has played a particularly significant role in the air-sea CO_2 flux variability over the last 3 decades, especially at longer timescales. To ascertain the mechanisms driving the CO_2 flux variability, it is insightful to investigate the processes governing the variation of $d\Delta pCO_2$. Because the relevant term ΔpCO_2 is determined by the imbalance between pCO_{2a} and pCO_{2o}, the $d\Delta pCO_2$ (i.e., $\Delta pCO_2 - \overline{\Delta pCO_2}$) is expressed as

$$\begin{aligned} d\Delta pCO_2 &= pCO_{2o} - pCO_{2a} - \left(\overline{pCO_{2o} - pCO_{2a}}\right) = pCO_{2o}{}' - pCO_{2a}{}', \\ \text{with } pCO_{2o}{}' &= pCO_{2o} - \overline{pCO_{2o}} \text{ and } pCO_{2a}{}' = pCO_{2a} - \overline{pCO_{2a}}. \end{aligned} \quad (12)$$

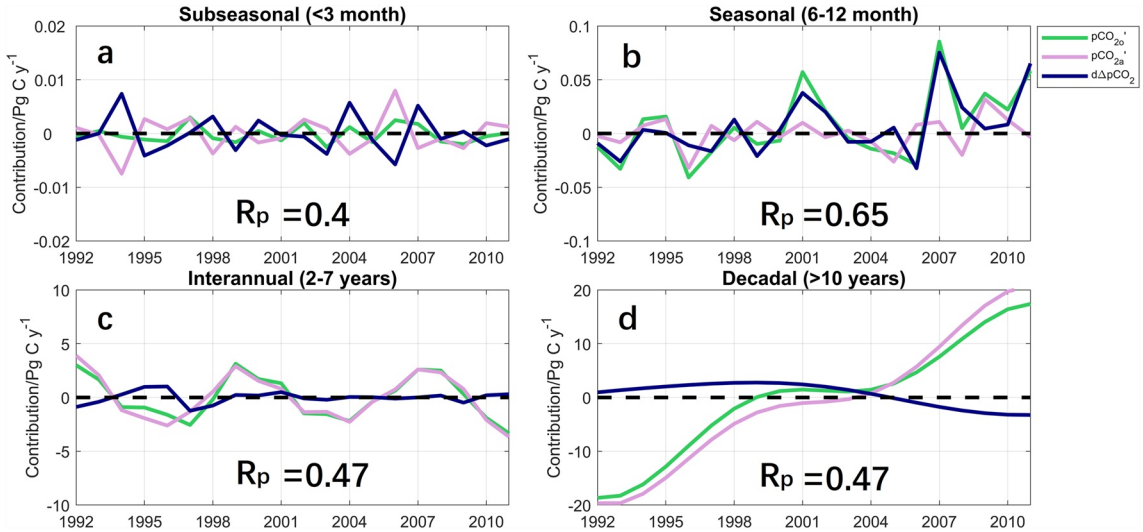

Figure 6. Time-series of the oceanic pCO_2 anomaly (pCO_{2o}', green), the atmospheric pCO_2 anomaly (pCO_{2a}', pink) and the anomaly of the difference in oceanic pCO_2 and atmospheric pCO_2 ($d\Delta pCO_2$, dark blue) from 1992 to 2010 on (a) subseasonal, (b) seasonal, (c) interannual, and (d) decadal timescales. Whole time-series (1988 and 2015) of pCO_{2a} and pCO_{2o} data are not plotted because the secular trend in these variables can lead to spurious extreme values at the beginning and end of the time-series analyses. The ratio R_p shown in the figure is calculated using Equation 13.

To quantify the relative strengths of pCO_{2a}' and pCO_{2o}', similarly, the ratio R_p is introduced and expressed as

$$R_p = \frac{|pCO_{2o}'|}{|pCO_{2o}'| + |pCO_{2a}'|}. \quad (13)$$

The resulting contribution of globally averaged pCO_{2a}' and pCO_{2o}' are smaller on subseasonal and seasonal time scales compared with longer time scales (Figure 6). $d\Delta pCO_2$ varies in opposing direction to pCO_{2a}' on subseasonal time scales because of the relatively weak variability of pCO_{2o}' ($R_p = 0.4$). Conversely, the weak variability of pCO_{2a}' ($R_p = 0.65$) leads $d\Delta pCO_2$ to generally follow pCO_{2o}' on seasonal timescales (Figures 6a and 6b). Both variabilities of pCO_{2a}' and pCO_{2o}' are amplified at higher latitudes (see the first two rows in Figure 7). The variation of pCO_{2o}' generally follows pCO_{2a}' globally with almost equivalent magnitude ($R_p \approx 0.5$) on interannual and decadal timescales, resulting in a small variability of global average $d\Delta pCO_2$ (Figures 6c and 6d), with some higher interannual and decadal variabilities in $d\Delta pCO_2$ within equatorial and high latitude regions, respectively (the third and fourth row in Figure 7). The global interannual variability of CO_2 flux mostly originates from Tropical Pacific (McKinley et al., 2004; Peylin et al., 2005) and the prominent and negative phase of $d\Delta pCO_2$ during 1997/1998 dominated by pCO_{2o}' is associated with El Niño events (the third row in Figure 7), consistent with other observation (McKinley et al., 2020).

On decadal timescales, the variability in global $d\Delta pCO_2$ is mostly driven by processes in high latitude regions (Figure 7), with the resulting ΔpCO_2 effect and flux anomaly reversing from positive to negative after 2005 (Figure 3d; Figures S1 and S3d in Supporting Information S1), explaining the CO_2 sink reinvigoration in the early 2000s. Specifically, a positive anomaly of ΔpCO_2 before 2005 is the result of a higher growth rate of oceanic pCO_2 than atmospheric pCO_2, especially in high latitude regions (Figures 6d and 7). The reduction of atmospheric pCO_2 growth rate relative to the oceanic pCO_2 is due in part to the volcano-forced SST variability after 1991 (McKinley et al., 2020), and the acceleration of oceanic pCO_2 growth rate in the Southern Ocean is associated with enhanced upwelling and meridional overturning circulation due to the southward shift and intensification of westerlies under the impact of the positive phase of Southern Annular Mode (DeVries et al., 2017; Le Quéré et al., 2007). After 2005, while the pCO_{2o}' is increasing sharply under the impact of nonthermal component of pCO_{2o}' (Figure 8d, see the discussion in next paragraph), it is increasing slower than pCO_{2a}', also mainly in high latitude regions for both northern and southern hemispheres (Figures 6d and 7). In the Southern Ocean, the reduction of oceanic pCO_2 growth rate occurred due to weaken overturning circulation, and/or the development of an asymmetric atmospheric pattern showing cooling in the Pacific sector and reduction of DIC because of enhanced stratification and reduced upwelling in the Atlantic sector (DeVries et al., 2017; Gruber et al., 2019; Landschützer

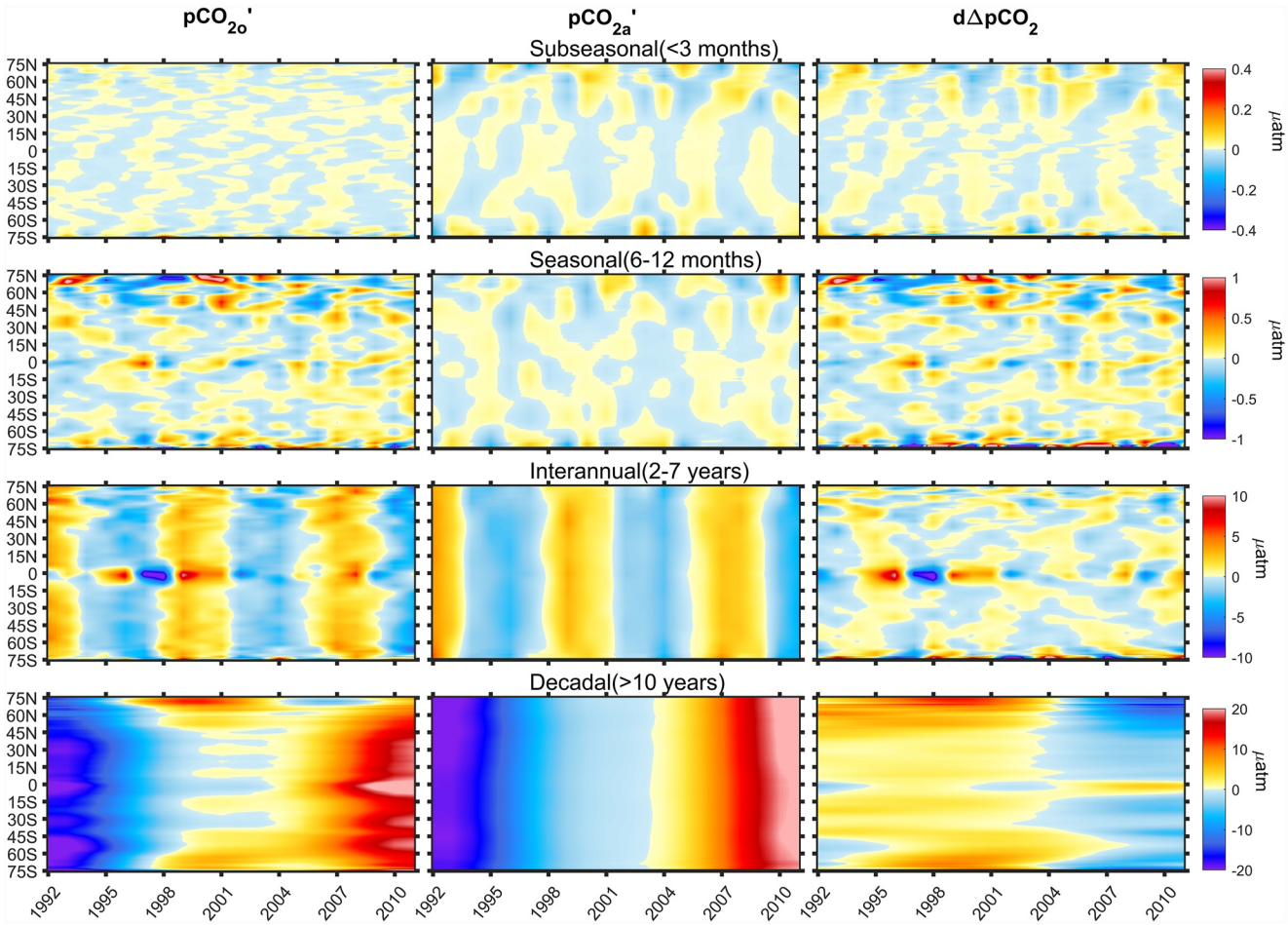

Figure 7. Hovmöller diagram of the distribution of the oceanic pCO_2 anomaly (pCO_{2o}', first column), the atmospheric pCO_2 anomaly (pCO_{2a}', second column) and the anomaly of the difference in oceanic pCO_2 and atmospheric pCO_2 ($d\Delta pCO_2$, third column) from 1992 to 2010 on various timescales (from top to bottom, subseasonal, seasonal, interannual and decadal timescales). Note that pCO_{2a}' is uniform in space but variable across years for decadal time scales.

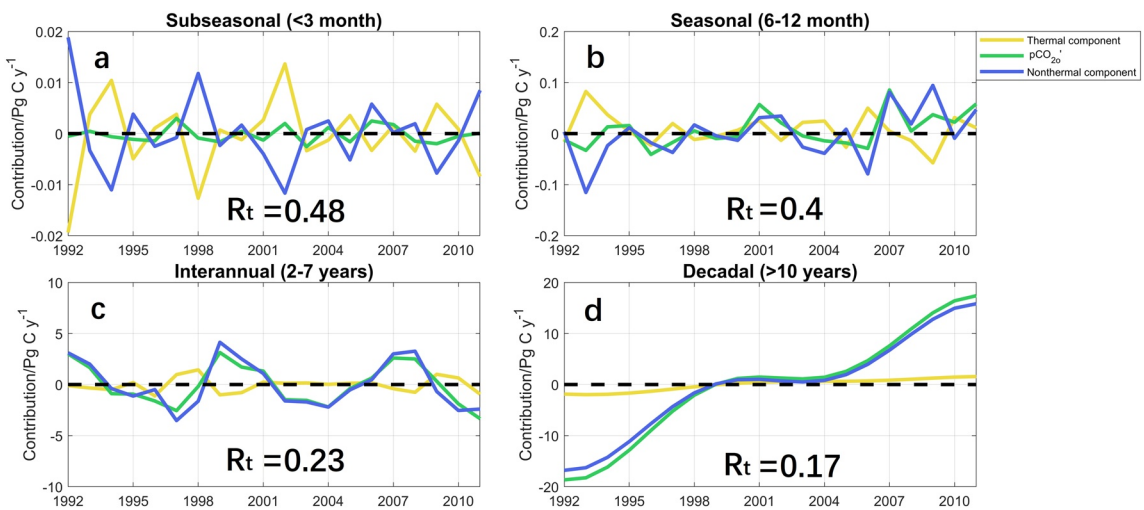

Figure 8. The contribution of the thermal (in yellow) and nonthermal (in blue) components of pCO_{2o}' and observed pCO_{2o}'(in green) from 1992 to 2010 on (a) subseasonal, (b) seasonal, (c) interannual, and (d) decadal timescales.

et al., 2015). In comparison, mechanisms driving changes of oceanic pCO_2 in the northern hemisphere are less investigated (Gruber et al., 2023).

In the ocean, pCO_{2o} is a function of DIC concentration, SST, ALK, and salinity (Sarmiento & Gruber, 2006). The effect of salinity on pCO_{2o} is comparatively small and can be neglected (Landschützer et al., 2014; Sarmiento & Gruber, 2006), though salinity may have regional impacts on short timescales and may delineate distinct biogeochemical regimes. Therefore, the focus here is on nonthermal (DIC and ALK) and thermal components (SST) as drivers of pCO_{2o}. The nonthermal component is broadly defined to include biological processes at the ocean surface (photosynthesis and respiration), and the vertical mixing of deep waters with a remineralization signal. The thermal component induced by variations in SST ($pCO_{2o}|'_{thermal}$) can be estimated based on the SST sensitivity following Sarmiento and Gruber (2006) and is given by

$$pCO_{2o}|'_{thermal} \approx pCO_{2o} \times 0.0423\,(^{\circ}C)^{-1} \times SST', \tag{14}$$

where the pCO_{2o} is the annual average oceanic pCO_2, SST′ is the SST anomaly computed by removing the long-term average SST from the annual average SST (i.e., $SST - \overline{SST}$). The nonthermal component of pCO_{2o} changes ($pCO_{2o}|'_{nonthermal}$) is thereby estimated by subtracting the thermal component from the observed annual oceanic pCO_2 anomaly (pCO_{2o}')

$$pCO_{2o}|'_{nonthermal} = pCO_{2o}' - pCO_{2o}|'_{thermal}. \tag{15}$$

Substantial variations in globally averaged thermal and nonthermal components of pCO_{2o}' and pCO_{2o}' are observed at all four timescales over the recent three decades (Figure 8). Quantitively, the ratio R_t is again used to evaluate the relative strengths of nonthermal and thermal components of pCO_{2o}'. In this context, the R_t is expressed as

$$R_t = \frac{|\text{thermal component}|}{|\text{thermal component}| + |\text{nonthermal component}|}. \tag{16}$$

On subseasonal timescales, the magnitude of the thermal component is comparable with the nonthermal component ($R_t \approx 0.5$) and the two variables tend to change in opposite directions, leading to a relatively stable pCO_{2o}'. In contrast, on longer timescales, R_t is smaller than 0.5 and decreases as timescales become longer, indicating that the nonthermal component becomes increasingly important compared to the thermal component. The consistent variability of nonthermal component and pCO_{2o}' suggests a dominant role of the nonthermal component in controlling the pCO_{2o}' distribution and variation over the global ocean on interannual ($R_t = 0.23$) and decadal ($R_t = 0.17$) timescales (Figures 8 and 9). It is worth noting that the pCO_2' signal on decadal timescales switches from negative to positive in year 2000 likely because of the enhancement in the thermal component resulting from the increasing SST and nonthermal component over the polar regions (see bottom panels of Figure 9). The sharp increase in pCO_{2o}' since the year of 2005 (Figure 8d) is likely produced by the prominent enhancement of the nonthermal component over the global ocean (Figure 9, bottom).

4. Limitations and Future Work

Air-sea CO_2 flux estimates carry uncertainties associated with the gas transfer velocity parameterizations, data products, poor spatial and temporal coverage of CO_2 data, thermal and haline effects and the non-linearity in wind dependence functions, to name a few (Bakker et al., 2014; Chiodi et al., 2019; Roobaert et al., 2018; Takahashi et al., 2014; Wanninkhof et al., 2002; Ward et al., 2004; Woolf et al., 2016, 2019). Among these, there is general agreement that data products and gas transfer velocity expressions remain important sources of uncertainties in air-sea CO_2 flux (Roobaert et al., 2018; Woolf et al., 2019). Similar results were obtained using two independent (wind-only and wind-wave) k parameterizations suggesting that the conclusions are insensitive to the choice of the gas transfer velocity expression. Though wave height is included in the wind-wave parameterization, wind speed and ΔpCO_2 effect remain the key drivers of CO_2 flux across temporal scales (Figure S3 in Supporting Information S1). To test the impact of using a different data product, we repeated the analyses using a pCO_2 data ensemble of six observation-based products from SeaFlux (Fay et al., 2021). These products include a mixed layer scheme product, a multiple linear regression, a machine-learning ensemble and three neural-network-derived products. The zonal distribution and the overall magnitude of driving factors exhibit a fundamental consistency

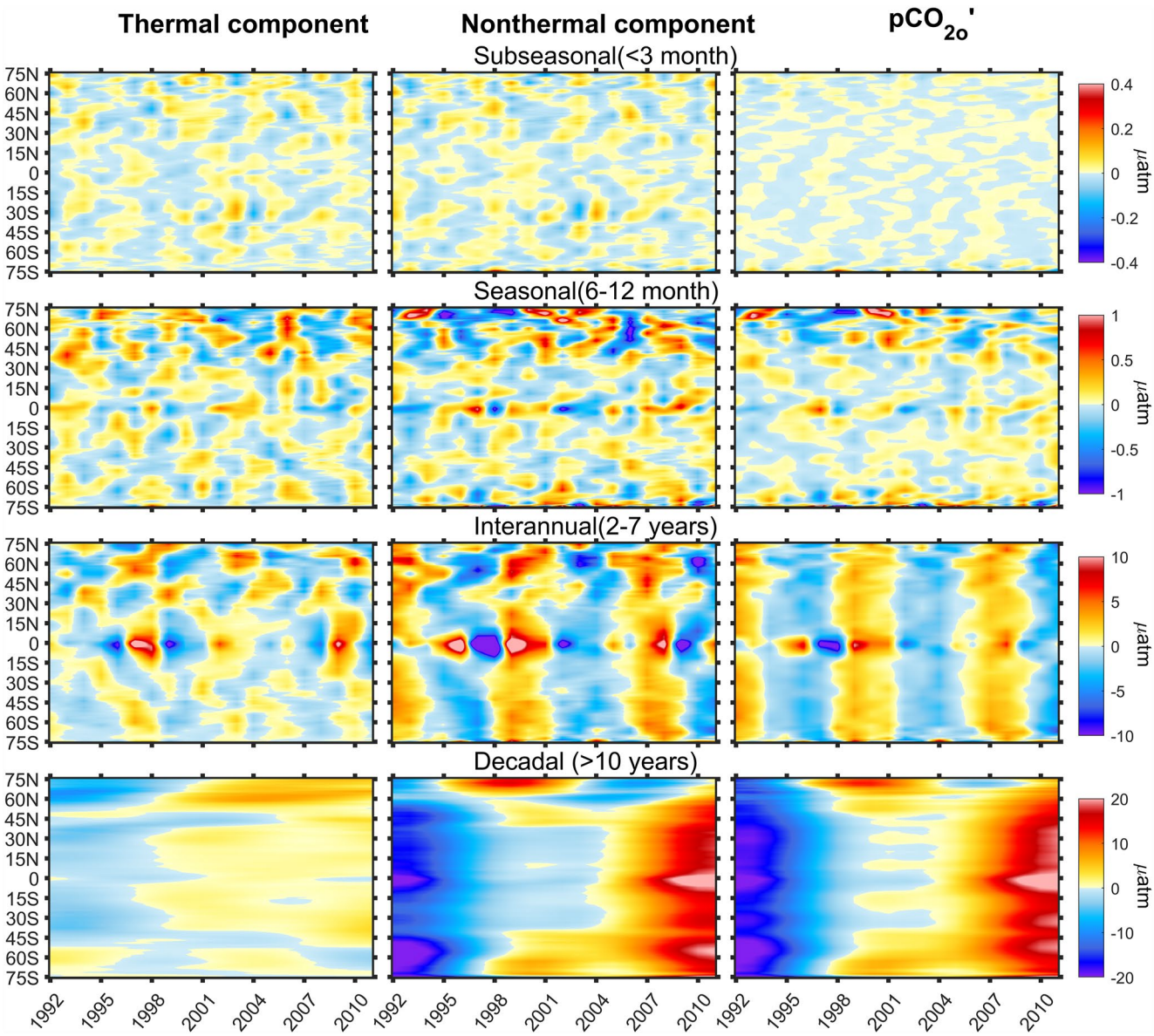

Figure 9. Hovmöller diagram of the distribution of thermal component (left) and nonthermal component (middle) of pCO_{2o}' and observed pCO_{2o}' (right) from 1992 to 2010 on various timescales (from top to bottom, subseasonal, seasonal, interannual, and decadal timescales).

across products, albeit with minor differences (Figures S7–S10 in Supporting Information S1). However, the results from these two pCO_2 products are not independent because they are both produced based on the SOCAT database. The increasing number of observations since the beginning of the 21st century have led to an improved characterization of the interannual and long-term variability of CO_2 fluxes. However, uncertainties in reconstructed pCO_2 products remain because of sparse sampling in some regions and at some times of the year (e.g., Southern Ocean austral winter). For example, the airborne observations by Long et al. (2021) challenge the profiling floats estimates of annual mean CO_2 uptake in the Southern Ocean (Bushinsky et al., 2019; Gray et al., 2018). This is partly attributable to aliasing associated with current sampling efforts often not capturing synoptic perturbations (1–10 days) such as storms (Djeutchouang et al., 2022; Nicholson et al., 2022). Considering the potential aliasing issues impacting the conclusions, the mass-preserving and variance-preserving approaches are both employed to analyze the multiscale temporal variability of CO_2 flux. The identical variability in the spectra for both approaches might indicate that the conclusions drawn from this work seem to be robust to the aliasing effect. However, this agreement is necessary but not sufficient. Caution must be maintained because the impact of these

synoptic events on subseasonal, and longer timescales carbon budgets remains an active area of research that cannot be settled with such comparisons between variance and mass preserving approaches.

5. Conclusions

The work presented here identifies and quantifies the factors (wind speed, ΔpCO_2, SST, and H_s) driving global air-sea CO_2 flux variability at a range of timescales (i.e., subseasonal, seasonal, interannual, and decadal timescales) using a data set from 1988 to 2015. Among other things, the results here can be used to evaluate and refine the representation of air-sea CO_2 flux in earth system models. On subseasonal timescales, the magnitude of CO_2 flux anomalies appeared lowest (Figure S1) and the variability is mainly driven by wind speed variability (~66%). On longer timescales (i.e., seasonal, interannual, and decadal timescales), the CO_2 flux variability was primarily controlled by the ΔpCO_2 effect. At all four timescales, the pattern of wind effect results from the product of a wind speed anomaly and ΔpCO_2. In contrast, the distribution of the ΔpCO_2 effects was primarily driven by the ΔpCO_2 anomaly ($d\Delta pCO_2$). The ΔpCO_2 anomaly itself was controlled by atmospheric pCO_2 variations and oceanic pCO_2 variations that are mainly driven by a nonthermal component, particularly on longer timescales. The lower growth rate of oceanic pCO_2 compared to atmospheric pCO_2, particularly in the high latitude regions after the year 2005, leads to an increased oceanic CO_2 sink on decadal timescales, which may be associated with variability in ocean circulation, biology and atmospheric forcing such as the Northern and Southern Annular Mode (DeVries, 2022; Gruber et al., 2019; Landschützer et al., 2016; Le Quéré et al., 2007; Lovenduski et al., 2008).

While wind is of second-order importance in controlling air-sea CO_2 flux at longer timescales, it may have a substantial indirect impact through its effect on vertical mixing and exchange with CO_2-rich deep waters. This is especially the case in the Southern Ocean, where air-sea CO_2 flux is impacted by wind location and speed on decadal timescales (Gruber et al., 2019; Keppler & Landschützer, 2019; Landschützer et al., 2015; Le Quéré et al., 2007; Lovenduski et al., 2008). In light of polar amplification of climatic changes, and the fact that the global patterns we observed at multiple temporal scales often stem from the Southern Ocean, increasing the number of air-sea CO_2 flux observations is urgently needed in polar regions. Their central role in the global carbon budget stands in sharp contrast with the limited observations currently available.

Conflict of Interest

The authors declare no conflicts of interest relevant to this study.

Data Availability Statement

The cross-calibrated multiplatform (CCMP-V2) 6-hourly wind speed are publicly available at www.remss.com/measurements/ccmp. The pCO_{2o}, pCO_{2a}, and ΔpCO_2 data were obtained from https://www.ncei.noaa.gov/access/ocean-carbon-datasystem/oceans/SPCO2_1982_2015_ETH_SOM_FFN.html. The significant wave height and sea surface temperature data were obtained from https://cds.climate.copernicus.eu/cdsapp#!/dataset/reanalysis-era5-single-levels?tab=overview. The SeaFlux pCO_2 data were obtained from https://zenodo.org/record/5482547#.YVdPeY5KhPY.

Acknowledgments
Y.G. is supported by a scholarship from the China Scholarship Council (CSC) under the Grant CSC 201906710071. G.K. acknowledges support from the U.S. National Science Foundation (NSF-AGS-2028633) and the Department of Energy, Office of Science (DE-SC0022072). N. C. is supported by the "Laboratoire d'Excellence" Labex-MER (ANR-10-LABX-19) and cofunded by a Grant from the French government under the program "Investissements d'Avenir."

References

Antonov, J. I., Seidov, D., Boyer, T. P., Locarnini, R. A., Mishonov, A. V., Garcia, H. E., et al. (2010). World Ocean Atlas 2009. In S. Levitus (Ed.), *NOAA Atlas NESDIS 69*, *Salinity* (Vol. 2, 184 pp.). U.S. Government Printing Office. Retrieved from http://www.nodc.noaa.gov/OC5/indprod.html

Arruda, R., Calil, P. H., Bianchi, A. A., Doney, S. C., Gruber, N., Lima, I., & Turi, G. (2015). Air-sea CO_2 fluxes and the controls on ocean surface pCO_2 seasonal variability in the coastal and open-ocean southwestern Atlantic Ocean: A modeling study. *Biogeosciences*, *12*(9), 5793–5809. https://doi.org/10.5194/bg-12-5793-2015

Atlas, R., Hoffman, R. N., Ardizzone, J., Leidner, S. M., Jusem, J. C., Smith, D. K., & Gombos, D. (2011). A cross-calibrated, multiplatform ocean surface wind velocity product for meteorological and oceanographic applications. *Bulletin of the American Meteorological Society*, *92*(2), 157–174. https://doi.org/10.1002/2017JC013181

Bakker, D. C. E., Pfeil, B., Smith, K., Hankin, S., Olsen, A., Alin, S. R., et al. (2014). An update to the Surface Ocean CO_2 Atlas (SOCAT version 2) [Dataset]. Earth System Science Data, *6*(1), 69–90. https://doi.org/10.5194/essd-6-69-2014

Brumer, S. E., Zappa, C. J., Blomquist, B. W., Fairall, C. W., Cifuentes-Lorenzen, A., Edson, J. B., et al. (2017a). Wave-related Reynolds number parameterizations of CO_2 and DMS transfer velocities. *Geophysical Research Letters*, *44*(19), 9865–9875. https://doi.org/10.1002/2017GL074979

Brumer, S. E., Zappa, C. J., Brooks, I. M., Tamura, H., Brown, S. M., Blomquist, B. W., et al. (2017b). Whitecap coverage dependence on wind and wave statistics as observed during SO GasEx and HiWinGS. *Journal of Physical Oceanography*, *47*(9), 2211–2235. https://doi.org/10.1175/JPO-D-17-0005.1

Bushinsky, S. M., Landschützer, P., Rödenbeck, C., Gray, A. R., Baker, D., Mazloff, M. R., et al. (2019). Reassessing Southern Ocean air-sea CO_2 flux estimates with the addition of biogeochemical float observations. *Global Biogeochemical Cycles*, *33*(11), 1370–1388. https://doi.org/10.1029/2019GB006176

Chau, T. T. T., Gehlen, M., & Chevallier, F. (2022). A seamless ensemble-based reconstruction of surface ocean pCO_2 and air–sea CO_2 fluxes over the global coastal and open oceans. *Biogeosciences*, *19*(4), 1087–1109. https://doi.org/10.5194/bg-19-1087-2022

Chiodi, A. M., Dunne, J. P., & Harrison, D. E. (2019). Estimating air-sea carbon flux uncertainty over the tropical Pacific: Importance of winds and wind analysis uncertainty. *Global Biogeochemical Cycles*, *33*(3), 370–390. https://doi.org/10.1029/2018GB006047

Couldrey, M. P., Oliver, K. I., Yool, A., Halloran, P. R., & Achterberg, E. P. (2016). On which timescales do gas transfer velocities control North Atlantic CO_2 flux variability? *Global Biogeochemical Cycles*, *30*(5), 787–802. https://doi.org/10.1002/2015GB005267

Deike, L., & Melville, W. K. (2018). Gas transfer by breaking waves. *Geophysical Research Letters*, *45*(19), 10–482. https://doi.org/10.1029/2018GL078758

De Verneil, A., Lachkar, Z., Smith, S., & Lévy, M. (2022). Evaluating the Arabian Sea as a regional source of atmospheric CO_2: Seasonal variability and drivers. *Biogeosciences*, *19*(3), 907–929. https://doi.org/10.5194/bg-19-907-2022

DeVries, T. (2022). Atmospheric CO_2 and sea surface temperature variability cannot explain recent decadal variability of the ocean CO_2 sink. *Geophysical Research Letters*, *49*(7), e2021GL096018. https://doi.org/10.1029/2021GL096018

DeVries, T., Holzer, M., & Primeau, F. (2017). Recent increase in oceanic carbon uptake driven by weaker upper-ocean overturning. *Nature*, *542*(7640), 215–218. https://doi.org/10.1038/nature21068

Djeutchouang, L. M., Chang, N., Gregor, L., Vichi, M., & Monteiro, P. (2022). The sensitivity of pCO_2 reconstructions to sampling scales across a Southern Ocean sub-domain: A semi-idealized ocean sampling simulation approach. *Biogeosciences*, *19*(17), 4171–4195. https://doi.org/10.5194/bg-19-4171-2022

Doney, S. C., Lima, I., Feely, R. A., Glover, D. M., Lindsay, K., Mahowald, N., et al. (2009). Mechanisms governing interannual variability in upper-ocean inorganic carbon system and air–sea CO_2 fluxes: Physical climate and atmospheric dust. *Deep Sea Research Part II: Topical Studies in Oceanography*, *56*(8–10), 640–655. https://doi.org/10.1016/j.dsr2.2008.12.006

Fay, A. R., Gregor, L., Landschützer, P., McKinley, G. A., Gruber, N., Gehlen, M., et al. (2021). SeaFlux: Harmonization of air–sea CO_2 fluxes from surface pCO_2 data products using a standardized approach. *Earth System Science Data*, *13*(10), 4693–4710. https://doi.org/10.5194/essd-2021-16

Feely, R. A., Takahashi, T., Wanninkhof, R., McPhaden, M. J., Cosca, C. E., Sutherland, S. C., & Carr, M. E. (2006). Decadal variability of the air-sea CO_2 fluxes in the equatorial Pacific Ocean. *Journal of Geophysical Research*, *111*(C8), C08S90. https://doi.org/10.1029/2005JC003129

Feely, R. A., Wanninkhof, R., Takahashi, T., & Tans, P. (1999). Influence of El Niño on the equatorial Pacific contribution to atmospheric CO_2 accumulation. *Nature*, *398*(6728), 597–601. https://doi.org/10.1038/19273

Fredriksen, H. B., & Rypdal, K. (2016). Spectral characteristics of instrumental and climate model surface temperatures. *Journal of Climate*, *29*(4), 1253–1268. https://doi.org/10.1175/JCLI-D-15-0457.1

Friedlingstein, P., O'sullivan, M., Jones, M. W., Andrew, R. M., Hauck, J., Olsen, A., et al. (2020). Global carbon budget 2020. *Earth System Science Data*, *12*(4), 3269–3340. https://doi.org/10.5194/essd-12-3269-2020

Goddijn-Murphy, L., Woolf, D. K., & Callaghan, A. H. (2011). Parameterizations and algorithms for oceanic whitecap coverage. *Journal of Physical Oceanography*, *41*(4), 742–756. https://doi.org/10.1175/2010JPO4533.1

Gray, A. R., Johnson, K. S., Bushinsky, S. M., Riser, S. C., Russell, J. L., Talley, L. D., et al. (2018). Autonomous biogeochemical floats detect significant carbon dioxide outgassing in the high-latitude Southern Ocean. *Geophysical Research Letters*, *45*(17), 9049–9057. https://doi.org/10.1029/2018GL078013

Gregor, L., & Fay, A. R. (2021). SeaFlux: Harmonised sea-air CO_2 fluxes from surface pCO_2 data products using a standardised approach [Dataset]. Zenodo. https://doi.org/10.5281/zenodo.5482547

Gruber, N., Bakker, D. C., DeVries, T., Gregor, L., Hauck, J., Landschützer, P., et al. (2023). Trends and variability in the ocean carbon sink. *Nature Reviews Earth & Environment*, *4*(2), 119–134. https://doi.org/10.1038/s43017-022-00381-x

Gruber, N., Landschützer, P., & Lovenduski, N. S. (2019). The variable Southern Ocean carbon sink. *Annual Review of Marine Science*, *11*(1), 159–186. https://doi.org/10.1146/annurev-marine-121916-063407

Hersbach, H., Bell, B., Berrisford, P., Biavati, G., Horányi, A., Muñoz Sabater, J., et al. (2018). ERA5 hourly data on single levels from 1979 to present [Dataset]. Copernicus Climate Change Service (C3S) Climate Data Store (CDS). https://doi.org/10.24381/cds.adbb2d47

Hoffman, R. N., Ardizzone, J. V., Leidner, S. M., Smith, D. K., & Atlas, R. (2013). Error estimates for ocean surface winds: Applying Desroziers diagnostics to the cross-calibrated, multiplatform analysis of wind speed. *Journal of Atmospheric and Oceanic Technology*, *30*(11), 2596–2603. https://doi.org/10.1175/JTECH-D-13-00018.1

Igarashi, Y., Katul, G. G., Kumagai, T. O., Yoshifuji, N., Sato, T., Tanaka, N., et al. (2015). Separating physical and biological controls on long-term evapotranspiration fluctuations in a tropical deciduous forest subjected to monsoonal rainfall. *Journal of Geophysical Research: Biogeosciences*, *120*(7), 1262–1278. https://doi.org/10.1002/2014JG002767

Iida, Y., Takatani, Y., Kojima, A., & Ishii, M. (2021). Global trends of ocean CO_2 sink and ocean acidification: An observation-based reconstruction of surface ocean inorganic carbon variables. *Journal of Oceanography*, *77*(2), 323–358. https://doi.org/10.1007/s10872-020-00571-5

Ishii, M., Feely, R. A., Rodgers, K. B., Park, G. H., Wanninkhof, R., Sasano, D., et al. (2014). Air–sea CO_2 flux in the Pacific Ocean for the period 1990–2009. *Biogeosciences*, *11*(3), 709–734. https://doi.org/10.5194/bg-11-709-2014

Jähne, B., Wais, T., Memery, L., Caulliez, G., Merlivat, L., Münnich, K. O., & Coantic, M. (1985). He and Rn gas exchange experiments in the large wind-wave facility of IMST. *Journal of Geophysical Research*, *90*(C6), 11989–11997. https://doi.org/10.1029/JC090iC06p11989

Keeling, R. F. (1993). On the role of large bubbles in air-sea gas exchange and supersaturation in the ocean. *Journal of Marine Research*, *51*(2), 237–271. https://doi.org/10.1357/0022240933223800

Keppler, L., & Landschützer, P. (2019). Regional wind variability modulates the Southern Ocean carbon sink. *Scientific Reports*, *9*(1), 1–10. https://doi.org/10.1038/s41598-019-43826-y

Komori, S., Nagaosa, R., & Murakami, Y. (1993). Turbulence structure and mass transfer across a sheared air–water interface in wind-driven turbulence. *Journal of Fluid Mechanics*, *249*(-1), 161–183. https://doi.org/10.1017/S0022112093001120

Landschützer, P., Gruber, N., & Bakker, D. C. (2016). Decadal variations and trends of the global ocean carbon sink. *Global Biogeochemical Cycles*, *30*(10), 1396–1417. https://doi.org/10.1002/2015GB005359

Landschützer, P., Gruber, N., Bakker, D. C., & Schuster, U. (2014). Recent variability of the global ocean carbon sink. *Global Biogeochemical Cycles*, *28*(9), 927–949. https://doi.org/10.1002/2014gb004853

Landschützer, P., Gruber, N., Bakker, D. C., Stemmler, I., & Six, K. D. (2018). Strengthening seasonal marine CO_2 variations due to increasing atmospheric CO_2. *Nature Climate Change*, *8*(2), 146–150. https://doi.org/10.1038/s41558-017-0057-x

Landschützer, P., Gruber, N., & Bakker, D. C. E. (2017). An updated observation-based global monthly gridded sea surface pCO2 and air-sea CO_2 flux product from 1982 through 2015 and its monthly climatology (NCEI Accession 0160558) (Version 2.2) [Dataset]. NOAA National Centers for Environmental Information. Retrieved from https://www.ncei.noaa.gov/access/ocean-carbon-acidification-data-system/oceans/SPCO2_1982_2015_ETH_SOM_FFN.html

Landschützer, P., Gruber, N., Haumann, F. A., Rödenbeck, C., Bakker, D. C., Van Heuven, S., et al. (2015). The reinvigoration of the Southern Ocean carbon sink. *Science*, *349*(6253), 1221–1224. https://doi.org/10.1126/science.aab2620

Large, W. B. (2006). Surface fluxes for practitioners of global ocean data assimilation. In E. P. Chassignet & J. Verron (Eds.), *Ocean weather forecasting*. Springer. https://doi.org/10.1007/1-4020-4028-8_9

Le Quéré, C., Orr, J. C., Monfray, P., Aumont, O., & Madec, G. (2000). Interannual variability of the oceanic sink of CO_2 from 1979 through 1997. *Global Biogeochemical Cycles*, *14*(4), 1247–1265. https://doi.org/10.1029/1999GB900049

Le Quéré, C., Rödenbeck, C., Buitenhuis, E. T., Conway, T. J., Langenfelds, R., Gomez, A., et al. (2007). Saturation of the Southern Ocean CO_2 sink due to recent climate change. *Science*, *316*(5832), 1735–1738. https://doi.org/10.1126/science.1136188

Lerner, P., Romanou, A., Kelley, M., Romanski, J., Ruedy, R., & Russell, G. (2021). Drivers of air-sea CO_2 flux seasonality and its long-term changes in the NASA-GISS model CMIP6 submission. *Journal of Advances in Modeling Earth Systems*, *13*(2), e2019MS002028. https://doi.org/10.1029/2019MS002028

Long, M. C., Lindsay, K., Peacock, S., Moore, J. K., & Doney, S. C. (2013). Twentieth-century oceanic carbon uptake and storage in CESM1 (BGC). *Journal of Climate*, *26*(18), 6775–6800. https://doi.org/10.1175/JCLI-D-12-00184.1

Long, M. C., Stephens, B. B., McKain, K., Sweeney, C., Keeling, R. F., Kort, E. A., et al. (2021). Strong Southern Ocean carbon uptake evident in airborne observations. *Science*, *374*(6572), 1275–1280. https://doi.org/10.1126/science.abi4355

Lovenduski, N. S., Gruber, N., & Doney, S. C. (2008). Toward a mechanistic understanding of the decadal trends in the Southern Ocean carbon sink. *Global Biogeochemical Cycles*, *22*(3). https://doi.org/10.1029/2007GB003139

Lovenduski, N. S., Gruber, N., Doney, S. C., & Lima, I. D. (2007). Enhanced CO_2 outgassing in the Southern Ocean from a positive phase of the Southern Annular Mode. *Global Biogeochemical Cycles*, *21*(2). https://doi.org/10.1029/2006GB002900

Madden, R. A., & Julian, P. R. (1971). Detection of a 40–50 day oscillation in the zonal wind in the tropical Pacific. *Journal of the Atmospheric Sciences*, *28*(5), 702–708. https://doi.org/10.1175/1520-0469(1971)028<0702:DOADOI>2.0.CO;2

McGillis, W. R., Edson, J. B., Zappa, C. J., Ware, J. D., McKenna, S. P., Terray, E. A., et al. (2004). Air-sea CO_2 exchange in the equatorial Pacific. *Journal of Geophysical Research*, *109*(C8). https://doi.org/10.1029/2003JC002256

McKinley, G. A., Fay, A. R., Eddebbar, Y. A., Gloege, L., & Lovenduski, N. S. (2020). External forcing explains recent decadal variability of the ocean carbon sink. *AGU Advances*, *1*(2), e2019AV000149. https://doi.org/10.1029/2019AV000149

McKinley, G. A., Fay, A. R., Lovenduski, N. S., & Pilcher, D. J. (2017). Natural variability and anthropogenic trends in the ocean carbon sink. *Annual Review of Marine Science*, *9*(1), 125–150. https://doi.org/10.1146/annurev-marine-010816-060529

McKinley, G. A., Fay, A. R., Takahashi, T., & Metzl, N. (2011). Convergence of atmospheric and North Atlantic carbon dioxide trends on multidecadal timescales. *Nature Geoscience*, *4*(9), 606–610. https://doi.org/10.1038/ngeo1193

McKinley, G. A., Follows, M. J., & Marshall, J. (2004). Mechanisms of air-sea CO_2 flux variability in the equatorial Pacific and the North Atlantic. *Global Biogeochemical Cycles*, *18*(2). https://doi.org/10.1029/2003GB002179

Nicholson, S. A., Whitt, D. B., Fer, I., du Plessis, M. D., Lebéhot, A. D., Swart, S., et al. (2022). Storms drive outgassing of CO_2 in the subpolar Southern Ocean. *Nature Communications*, *13*(1), 158. https://doi.org/10.1038/s41467-021-27780-w

Nightingale, P. D., Malin, G., Law, C. S., Watson, A. J., Liss, P. S., Liddicoat, M. I., et al. (2000). In situ evaluation of air-sea gas exchange parameterizations using novel conservative and volatile tracers. *Global Biogeochemical Cycles*, *14*(1), 373–387. https://doi.org/10.1029/1999GB900091

Peylin, P., Bousquet, P., Le Quéré, C., Sitch, S., Friedlingstein, P., McKinley, G., et al. (2005). Multiple constraints on regional CO_2 flux variations over land and oceans. *Global Biogeochemical Cycles*, *19*(1). https://doi.org/10.1029/2003GB002214

Prytherch, J., Yelland, M. J., Pascal, R. W., Moat, B. I., Skjelvan, I., & Srokosz, M. A. (2010). Open ocean gas transfer velocity derived from long-term direct measurements of the CO_2 flux. *Geophysical Research Letters*, *37*(23). https://doi.org/10.1029/2010GL045597

Roobaert, A., Laruelle, G. G., Landschützer, P., Gruber, N., Chou, L., & Regnier, P. (2019). The spatiotemporal dynamics of the sources and sinks of CO_2 in the global coastal ocean. *Global Biogeochemical Cycles*, *33*(12), 1693–1714. https://doi.org/10.1029/2019GB006239

Roobaert, A., Laruelle, G. G., Landschützer, P., & Regnier, P. (2018). Uncertainty in the global oceanic CO_2 uptake induced by wind forcing: Quantification and spatial analysis. *Biogeosciences*, *15*(6), 1701–1720. https://doi.org/10.5194/bg-15-1701-2018

Sarmiento, J. L., & Gruber, N. (2006). *Ocean biogeochemical dynamics*. Princeton University Press. https://doi.org/10.2307/j.ctt3fgxqx

Sitch, S., Friedlingstein, P., Gruber, N., Jones, S. D., Murray-Tortarolo, G., Ahlström, A., et al. (2015). Recent trends and drivers of regional sources and sinks of carbon dioxide. *Biogeosciences*, *12*(3), 653–679. https://doi.org/10.5194/bg-12-653-2015

Staniec, A., Vlahos, P., & Monahan, E. C. (2021). The role of sea spray in atmosphere–ocean gas exchange. *Nature Geoscience*, *14*(8), 593–598. https://doi.org/10.1038/s41561-021-00796-z

Stull, R. B. (1988). *An introduction to boundary layer meteorology* (Vol. 13, 650 pp.). Springer Science & Business Media.

Takahashi, T., Feely, R. A., Weiss, R. F., Wanninkhof, R. H., Chipman, D. W., Sutherland, S. C., & Takahashi, T. T. (1997). Global air-sea flux of CO_2: An estimate based on measurements of sea–air pCO_2 difference. *Proceedings of the National Academy of Sciences*, *94*(16), 8292–8299. https://doi.org/10.1073/pnas.94.16.8292

Takahashi, T., Sutherland, S. C., Chipman, D. W., Goddard, J. G., Ho, C., Newberger, T., et al. (2014). Climatological distributions of pH, pCO_2, total CO_2, alkalinity, and $CaCO_3$ saturation in the global surface ocean, and temporal changes at selected locations. *Marine Chemistry*, *164*, 95–125. https://doi.org/10.1016/j.marchem.2014.06.004

Takahashi, T., Sutherland, S. C., Feely, R. A., & Cosca, C. E. (2003). Decadal variation of the surface water pCO_2 in the western and central equatorial Pacific. *Science*, *302*(5646), 852–856. https://doi.org/10.1126/science.1088570

Takahashi, T., Sutherland, S. C., Sweeney, C., Poisson, A., Metzl, N., Tilbrook, B., et al. (2002). Global sea–air CO_2 flux based on climatological surface ocean pCO_2, and seasonal biological and temperature effects. *Deep Sea Research Part II: Topical Studies in Oceanography*, *49*(9–10), 1601–1622. https://doi.org/10.1016/S0967-0645(02)00003-6

Takahashi, T., Sutherland, S. C., Wanninkhof, R., Sweeney, C., Feely, R. A., Chipman, D. W., et al. (2009). Climatological mean and decadal change in surface ocean pCO_2, and net sea–air CO_2 flux over the global oceans. *Deep Sea Research Part II: Topical Studies in Oceanography*, *56*(8–10), 554–577. https://doi.org/10.1016/j.dsr2.2008.12.009

Wanninkhof, R. (1992). Relationship between wind speed and gas exchange over the ocean. *Journal of Geophysical Research*, *97*(C5), 7373–7382. https://doi.org/10.1029/92JC00188

Wanninkhof, R. (2014). Relationship between wind speed and gas exchange over the ocean revisited. *Limnology and Oceanography: Methods*, *12*(6), 351–362. https://doi.org/10.4319/lom.2014.12.351

Wanninkhof, R., Doney, S. C., Takahashi, T., & Mcgillis, W. R. (2002). The effect of using time-averaged winds on regional air-sea CO_2 fluxes. *Geophysical Monograph-American Geophysical Union*, *127*, 351–356. https://doi.org/10.1029/GM127p0351

Wanninkhof, R., Park, G. H., Takahashi, T., Sweeney, C., Feely, R., Nojiri, Y., et al. (2013). Global ocean carbon uptake: Magnitude, variability and trends. *Biogeosciences*, *10*(3), 1983–2000. https://doi.org/10.5194/bg-10-1983-2013

Ward, B., Wanninkhof, R., McGillis, W. R., Jessup, A. T., DeGrandpre, M. D., Hare, J. E., & Edson, J. B. (2004). Biases in the air-sea flux of CO_2 resulting from ocean surface temperature gradients. *Journal of Geophysical Research*, *109*(C8). https://doi.org/10.1029/2003JC001800

Weiss, R. (1974). Carbon dioxide in water and seawater: The solubility of a non-ideal gas. *Marine Chemistry*, *2*(3), 203–215. https://doi.org/10.1016/0304-4203(74)90015-2

Woolf, D. K., Land, P. E., Shutler, J. D., Goddijn-Murphy, L. M., & Donlon, C. J. (2016). On the calculation of air-sea fluxes of CO_2 in the presence of temperature and salinity gradients. *Journal of Geophysical Research: Oceans*, *121*(2), 1229–1248. https://doi.org/10.1002/2015JC011427

Woolf, D. K., Shutler, J. D., Goddijn-Murphy, L., Watson, A. J., Chapron, B., Nightingale, P. D., et al. (2019). Key uncertainties in the recent air-sea flux of CO_2. *Global Biogeochemical Cycles*, *33*(12), 1548–1563. https://doi.org/10.1029/2018GB006041

Wrobel, I. (2017). Monthly dynamics of carbon dioxide exchange across the sea surface of the Arctic Ocean in response to changes in gas transfer velocity and partial pressure of CO_2 in 2010. *Oceanologia*, *59*(4), 445–459. https://doi.org/10.1016/j.oceano.2017.05.001

Zhang, M., Cheng, Y., Bao, Y., Zhao, C., Wang, G., Zhang, Y., et al. (2022). Seasonal to decadal spatiotemporal variations of the global ocean carbon sink. *Global Change Biology*, *28*(5), 1786–1797. https://doi.org/10.1111/gcb.16031

Zhao, D., & Toba, Y. (2001). Dependence of whitecap coverage on wind and wind-wave properties. *Journal of Oceanography*, *57*(5), 603–616. https://doi.org/10.1023/A:1021215904955